

1

1 **Assessment of the Finite VolumE Sea Ice Ocean Model** 2 **(FESOM2.0), Part II: Partial bottom cells, embedded sea ice and** 3 **vertical mixing library CVMix**

4
5 Patrick Scholz¹, Dmitry Sidorenko¹, Sergey Danilov^{1,2}, Qiang Wang¹, Nikolay Koldunov¹, Dmitry
6 Sein^{1,4}, Thomas Jung^{1,3}

7
8 ¹ Alfred Wegener Institute Helmholtz Center for Polar and Marine Research (AWI), Bremerhaven, Germany

9 ² Jacobs University Bremen, Department of Mathematics & Logistics, Bremen, Germany

10 ³ University of Bremen, Department of Physics and Electrical Engineering, Bremen, Germany

11 ⁴ Shirshov Institute of Oceanology, Russian Academy of Science, 36 Nahimovskiy Prospect, Moscow, Russia 117997

12
13 Correspondence to: Patrick Scholz (Patrick.Scholz@awi.de)

14 15 **Abstract**

16 The second part of the assessment and evaluation of the unstructured-mesh Finite-volumE Sea ice-Ocean
17 Model version 2.0 (FESOM2.0) is presented. It focuses on the performance of partial cells, embedded sea ice
18 and on the effect of mixing parameterisations available through the CVMix package.

19 It is shown that partial cells and embedded sea ice lead to significant improvements in the representation of
20 the Gulf Stream and North Atlantic Current as well as the circulation of the Arctic Ocean. In addition to the
21 already existing Pacanowski and Phillander (fesom_PP) and K-profile (fesom_KPP) parameterisations for
22 vertical mixing in FESOM2.0, we document the impact of several mixing parameterisations from the
23 Community Vertical Mixing (CVMix) project library. Among them are the CVMix versions of Pacanowski
24 and Phillander (cvmix_PP) and K-profile (cvmix_KPP) parameterisations, the tidal mixing parameterisation
25 (cvmix_TIDAL), a vertical mixing parameterisation based on turbulent kinetic energy (cvmix_TKE) as well
26 as a combination of cvmix_TKE and the recent scheme for the computation of the Internal Wave
27 Dissipation, Energy and Mixing (IDEMIX). IDEMIX parameterises the redistribution of internal wave
28 energy through wave propagation, nonlinear interactions and the associated imprint on the vertical
29 background diffusivity. Further, the benefit from using a parameterisation of southern hemisphere sea ice
30 melt season mixing in the surface layer (MOMIX) for reducing Southern Ocean hydrographic biases in
31 FESOM2.0 is presented. We document the implementation of different model components and illustrate their
32 behaviour. This paper serves primarily as a reference for FESOM users but is also useful to the broader
33 modelling community.

34 **1 Introduction**

35 Global unstructured-mesh ocean models start to be widely used in climate studies, including the recent
36 CMIP6 simulations (Semmler et al., 2020), although structured-mesh ocean general circulation models are
37 still more mature in terms of features, functionality and complexity due to their long development history.

2

1

38 However, step by step, also the unstructured-mesh ocean models acquire new features and catch up in their
39 functionality. This paper continues the work by Scholz et al. (2019) in documenting the features available in
40 Finite volumE Sea ice Ocean Model version 2.0 (FESOM2.0, Danilov et al., 2017). It focuses on two
41 aspects. The first is about partial bottom cells and embedded sea ice, both of which essentially rely on the
42 Arbitrary Lagrangian Eulerian (ALE) vertical coordinates used in FESOM2.0. The second deals with mixing
43 parameterizations enabled through the use of Community Ocean Vertical Mixing (CVMix, Griffies et al.
44 2015, Van Roekel et al. 2018) package.

45 Partial bottom cells were first introduced for a finite volume model by Adcroft et al., (1997), as an attempt to
46 improve the representation of the bottom topography in general ocean circulation models. Adcroft et al.,
47 (1997) introduces partial bottom cells as a compromise solution between the less accurate but
48 computationally efficient full cell approach and the very accurate but computationally expensive shaved cell
49 approach. Partial bottom cells are implemented in FESOM2.0 by using the vertical ALE approach of
50 FESOM2.0 numerical core documented in Danilov et al. 2017.

51 Another feature made available through using ALE in FESOM2.0 is related to the sea ice-ocean interaction.
52 Naturally, sea ice, more precisely the loading of sea ice, contributes to the ocean pressure. However in many
53 ocean models, especially in the absence of surface mass fluxes or on fixed vertical grids, the loading is
54 omitted and sea ice is treated as “levitating”. The option to consider sea ice loading is now implemented into
55 FESOM2.0, which is called “embedded” sea ice and was first mentioned by Hibler et al. (1998) and later
56 further introduced by Hutchings et al. (2005) and Campin et al. (2008). They state that the advection of sea
57 ice in combination with the coupling of “embedded” sea ice through ice loading can be an important source
58 of ocean variability especially in the vicinity of ice edges (Campin et al. 2008). The implementation of
59 embedded sea ice relies on the zstar vertical-coordinate option in FESOM2 and also on the fact that in the
60 moment the sea ice component is called on each time step of the ocean model using the standard EVP
61 method of Hunke and Dukowicz (1997) applying 150 EVP subcycles (Koldunov et al. 2019).

62 Diapycnal mixing in the ocean is an essential process that acts on the ocean stratification and the distribution
63 of heat, salt as well as passive tracers like nutrients, biological agents or CO₂. Various processes contributing
64 to diapycnal mixing can act with different magnitudes over a wide range of horizontal and vertical scales,
65 from several kilometers down to centimeters (Robertson and Dong, 2019). Due to the finite discretisation
66 scale in all ocean models, the mixing processes can not be resolved and thus must be parameterized. The
67 parameterisations of diapycnal mixing can be done in a variety of ways with different complexity, such as
68 boundary layer schemes like the K-profile parameterisation of Large et al. (1994) or turbulent closure
69 schemes like the one of Gaspar et al. 1990 and many others. A great innovation in the ocean modelling
70 community is the development of software packages that contain a variety of vertical mixing
71 parameterisations in a format that makes it easy to integrate them into existing model code (Fox Kemper et
72 al. 2019). One of these software packages is the Community Ocean Vertical Mixing package (CVMix,
73 Griffies et al. 2015, Van Roekel et al. 2018), which now also was integrated into FESOM2.0. CVMix is

74 tailored to be used in state of the art climate models to produce vertical profiles of diffusivity and viscosity
75 (Fox Kemper et al. 2019), providing a comparable mixing implementation over a wide spread of different
76 ocean models such as MOM6, POP, MPAS and ICON. Such effort makes it easier to compare these models
77 to each other. From the CVMix package we implemented the Pacanowski and Philander 1981, the K-profile
78 parameterization of Large et al. 1994 and the tidal mixing parameterisation of Simmons et al. 2004. Further,
79 the infrastructure of the CVMix library has been used to implement the turbulent kinetic energy (TKE)
80 scheme of Gaspar et al. (1990) and the scheme for Internal Wave Dissipation and Mixing (IDEMIX) of
81 Olbers and Eden (2013) in the same way as it is done in Gutjahr et al. (2020). It should be mentioned that
82 neither TKE nor IDEMIX is yet part of the official CVMix package but will hopefully be added to the
83 package in the future.

84 Beside the prime vertical mixing schemes, like the K-profile scheme, the Pacanowski and Phillander scheme
85 and others that have the purpose to create a general mixing parameterisation for the entire ocean, and vertical
86 mixing schemes like the tidal mixing scheme of Simmons et al. 2004 or IDEMIX that are used to
87 parametrize internal wave processes which then result in a heterogeneous background diffusivity, there are
88 also mixing parameterizations that aim at resolving regional processes. One of them was proposed by
89 Timmerman and Beckmann (2004). It parameterises the wind driven mixing in the Southern Ocean
90 especially when there is insufficient mixing during the melt seasons when other mixing schemes are used. It
91 is used in FESOM2.0 to improve the otherwise too low stratification in the Southern Ocean and Weddell
92 Sea.

93 The intention of this paper is to document the performance of the newly implemented features -- partial
94 bottom cells, “embedded” sea ice, the vertical mixing parameterisations that come with the implementation
95 of CMVIX and the local mixing parameterization of Timmerman and Beckmann (2004), based on comparing
96 the associated hydrographic biases, changes in vertical convection and differences in Meridional Overturning
97 Circulation, using a relatively coarse reference mesh.

98 The paper is structured as follows. First in Section 2 we describe the mesh configuration and model setup
99 used in the simulations. The description and analysis of partial bottom cells, “embedded” sea ice and vertical
100 mixing schemes is done in Section 3. A discussion and conclusion is given in Section 4.

101 **2 Model configurations**

102 We use the FESOM2.0 coarse mesh configuration core2, which is the same mesh as in part 1. It consists of
103 ~0.13M surface vertices, with a nominal resolution of 1° in the bulk of the ocean, ~25km north of 50°N , $1/3^\circ$
104 in the equatorial belt and slightly enhanced resolution in the coastal regions. In the vertical, 48 unevenly
105 distributed layers are used, with a vertical grid spacing stepwise increasing from 5m at the surface to 250 m
106 towards the bottom.

107 All model simulations are initialised from the Polar Science Center Hydrographic winter Climatology
108 (PHC3.0, updated from Steele et al., 2001) and forced by the CORE interannually varying atmospheric

109 forcing fields (Large and Yeager, 2009) for the period 1948-2009. For each simulation a spin-up over three
110 full CORE cycles was applied, where each subsequent cycle was initialised with the final results from the
111 preceding cycle. All modelled data shown in this work are averaged over the period 1989-2009.

112

113 All model simulations except the one with the Turbulent-Kinetic-Energy (TKE) closure mixing of Gaspar et
114 al., 1990, use a non-constant latitude-dependent vertical background diffusivity with values between 10^{-4}
115 m^2/s and $10^{-6} \text{m}^2/\text{s}$, as described in Scholz et al., 2019. Further, all simulations use the Monin-Obukhov
116 length dependent vertical mixing parameterization of Timmermann and Beckmann, 2004 in the surface
117 boundary layer south of -50°S . The effects of this parameterisation on the simulated ocean state in
118 FESOM2.0 is described in section 3.4. The horizontal viscosity is computed via a modified harmonic Leith
119 approach (Fox-Kemper and Menemenlis, 2008) plus a biharmonic background viscosity ($0.01 \text{m}^2/\text{s}$). For
120 coarse-mesh setups, like the one used here, FESOM2.0 uses the Gent-McWilliams (GM) parameterisation
121 for eddy stirring (Gent et al., 1995; Gent and McWilliams, 1990) and we follow the implementation after
122 Ferrari et al., 2010. The isoneutral tracer diffusion (Redi, 1982) coefficient equals to that of GM, same as in
123 Scholz et al. (2019) and in previous FESOM versions (Wang et al. 2014). GM and Redi are scaled with
124 horizontal resolution with a maximum value of $3000 \text{m}^2/\text{s}$ at 100 km horizontal resolution and change
125 linearly to zero between a resolution of 40 km and 30 km. In the vertical, they are scaled according to Ferrari
126 et al., 2010 and Wang et al., 2014. The simulations use as default the K-profile parameterisation for vertical
127 mixing (KPP, Large et al., 1994), a linear free surface (Scholz et al., 2019), levitating sea ice and a full
128 bottom cell approaches, unless otherwise stated.

129 **3 FESOM2.0 model components and evaluation**

130 **3.1 Partial bottom cells**

131 The concept of partial cells, as an attempt to improve the bottom representation in general ocean circulation
132 models was first introduced for the finite volume approach by Adcroft et al., (1997). Although an early
133 version of partial cells was developed by Cox, (1977), and used by Semtner and Mintz, (1977) and Maier-
134 Reimer et al., (1993), it has never got officially released (Griffies et al., 2000). Adcroft et al.
135 (1997) presented three different cases. The first one is the conventional full cell approach, where the depth of
136 the ocean bottom is approximated with the nearest standard depth level of the vertical model discretization.
137 The second one is the partial cell approach in which the bottom level can take any intermediate depth within
138 the cell, thus capturing water columns more accurately. In these two cases, the bottom features a “stepped”
139 topography and the jump of the steps is smaller for the partial cell approach (Adcroft et al., 1997). The third
140 case introduced by Adcroft et al., (1997) is a shaved cell approach, which assumes a constant slope within
141 each bottom cell and gives the best approximation for a continuous bottom topography. Adcroft et al.
142 (1997) showed that the shaved cell approach gives the most accurate results, but induces a significant

143 increase in computational demand, whereas the partial cell approach is a good compromise between the low
144 computational demand of the full cell approach and the increased accuracy of the shaved cell approach.
145 Hence, most ocean models (e.g. NEMO, MOM6, MPAS, POP) including FESOM2.0 went in favor of the
146 partial cell approach.

147 For the implementation of partial cells in FESOM2.0 we follow the work of Pacanowski and Gnanadesikan,
148 (1998), which implemented partial cells for the B-grid discretization in MOM2 with efforts to minimize
149 pressure gradient errors and spurious diapycnal mixing. They addressed that calculating horizontal pressure
150 gradients needs some special attention for partial cells since not all grid points within the bottom layer are at
151 the same depth. In FESOM2.0, we compute pressure gradient force based on the density Jacobian approach
152 as used by Shchepetkin, (2003) and not the pressure Jacobian approach proposed by Pacanowski and
153 Gnanadesikan, (1998). The density Jacobian approach is less prone to pressure-gradient error than using
154 pressure Jacobian, and therefore the model is more stable. Furthermore, we limited the thickness of the
155 partial bottom cell to be at least half of the full cell layer thickness to reduce the possibility of violating the
156 vertical Courant–Friedrichs–Lewy (CFL) criterion especially in shallow regions.

157 Using a B-grid like discretisation, where the scalars are located at vertices of a triangular mesh while the
158 velocities are located at the centroids of the triangular elements, makes it necessary to define the partial cells
159 at both locations. First, the partial bottom depth is defined at the centroids of the triangular elements based
160 on the real bottom topography considering the aforementioned limitation. Then, the vertex partial bottom
161 depth is derived from the deepest partial bottom of the surrounding triangular elements (see schematic
162 representation in Suppl. 1).

163 In order to demonstrate the effect of the partial cells on the simulated ocean state we performed two model
164 simulations using the full cell and partial cell approaches, respectively. We investigate, first, the temperature
165 biases of the full cell approach with respect to the data of the World Ocean Atlas 2018 (WOA18, Locarnini
166 et al., 2018; Zweng et al., 2018, in the left column of Fig. 1) and, second, the temperature differences
167 between partial cell and full cell (partial-full) averaged over five different depth ranges 0-250m, 250-500m,
168 500-1000m, 1000-2000m and 2000-4000m (in the right column of Fig. 1).

169 The full cell setup (Fig. 1, left) shows positive climatological temperature bias in the northern and southern
170 Pacific, the Atlantic equatorial ocean as well as in the central Indian Ocean through the depth ranges of 0-
171 250m, 250-500m and 500-1000m. In the same depth ranges there are also negative biases in the North
172 Atlantic (NA) subtropical gyre and in the equatorial and southern subtropical Pacific. The depth ranges of
173 250-500m and 500-1000m indicate cold biases in the Southern Ocean (SO) and around the coast of
174 Antarctica. The deeper depth ranges (1000-2000m and 2000-4000m.) indicate small negative temperature
175 biases in most of the world oceans, except for the Atlantic and Arctic Ocean (AO), which possess a small
176 warming bias in the depth ranges. The Arctic warming anomaly at these depths originates largely from a
177 vertically too much extended Atlantic water inflow branch (not shown), which is a typical feature of coarse
178 resolution models (e.g., Ilicak et al. 2016).

179 Using partial cells (Fig. 1, right) leads to profound changes especially at the position of zonal fronts in the
180 North and South Atlantic. In the depth ranges of 0-250 m, 250-500 m and 500-1000 m in the NA, partial
181 cells lead to a cooling in the Labrador Sea (LS) and Irminger Sea (IS) as well as along the path of the Gulf
182 Stream (GS) and North Atlantic Current (NAC), except for the area around -30°W , 50°N which is
183 characterised by warming. In the upper South Atlantic (SA), partial cells lead to a northward shift of Brazil–
184 Malvinas Confluence Zone expressed by a dipole of warmer South Atlantic Current (SAC) and cooler
185 Antarctic Circumpolar Current (ACC). Further, partial cells lead to a predominant cooling in the SO Atlantic
186 sector and parts of the Indian Ocean sector, while the Pacific sector of the SO and most of the Antarctic
187 coastal areas are dominated mostly by warming anomalies. The Arctic Ocean features a slight warming
188 anomaly at all depths, except for the surface, when using partial cells instead of full cells. The table in Suppl.
189 2 shows the regional ($-80^{\circ}\text{W} < \text{lon} < 5^{\circ}\text{E}$, $35^{\circ}\text{N} < \text{lat} < 70^{\circ}\text{N}$) temperature standard deviation and root mean
190 square error with respect to WOA18, with and without partial cells. It proves that partial cell lead to a
191 significant improvement especially in the upper and intermediate ocean depth range, while the biases in the
192 very deep ocean marginally increase.

193 Fig. 2 shows the same as Fig. 1 but for salinity. Here, with respect to WOA18, the full cell run indicates a
194 generally fresher AO for the surface- and the 250-500 m depth range. Further negative salinity biases can be
195 found within the upper three depth ranges in the equatorial Pacific, north and south subtropical Atlantic, at
196 the position of the Atlantic northwest corner, northern IO as well as parts of the SO. Strong positive salinity
197 biases with full cells can be found in the surface depth range of the North Pacific and in the Chukchi- and
198 Beaufort Sea. Further positive salinity biases in the 250-500 m and 500-1000 m depth ranges are found along
199 the pathway of the Gulf Stream as well as in the equatorial Atlantic and central IO. The deep depth range of
200 1000-2000m has positive salinity anomalies in the Northern and Southern Atlantic and negative salinity
201 biases in the Mediterranean outflow branch and IO.

202 Using partial cells leads to an increase in salinity throughout all depth ranges of the AO relative to using full
203 cells. Further, a salinity increase at the position of the “cold blob”, in the GIN sea, in the eastern South
204 Atlantic and parts of the SO can be observed within the upper three depth ranges. Compared to full cells,
205 using partial cells reduces salinity along the pathway of the GS, the Antarctic Circumpolar Current (ACC) in
206 the South Atlantic and along the coast of Antarctica.

207 The differences in the horizontal velocity speed between partial and full cells (Fig. 3), for the depth ranges of
208 0-250 m, 250-500 m, 500-1000 m, 1000-2000 m, 2000-4000 m and at the bottom, reveal that with partial
209 cells the velocity in the East Greenland Current (EGC), West Greenland Current (WGC) and Labrador
210 Current (LC) are stronger by up to 0.02 m/s through all depth ranges presented here. The upper differences
211 reveal that partial cells lead to a weakening and a slight southwards shift of the NAC between -45°W and -
212 30°W , and a more pronounced tendency towards a northwest bend of the NAC between -30°W and -15°W ,
213 which is nevertheless still too far eastward. By using partial cells the pathway of the Irminger Current (IC)
214 moves closer to the continental slope.

215 In terms of absolute northern and southern hemispheric maximum mixed layer depth (MLD), using full cell
216 (Fig. 4a and 4b), FESOM2.0 features known intensive convection in the Labrador Sea and Irminger Sea,
217 northern Greenland Sea as well as central Weddell Sea (Marshall and Schott 1999, Sallée et al. 2013,
218 Danabasoglu et al. 2014).

219 The anomalous northern and southern hemispheric maximum mixed layer depth (MLD), using partial cells
220 features a slight MLD decrease in the southern LS, IS and northern Greenland-Iceland-Norwegian (GIN)
221 Seas, and a slight MLD increase along the pathway of the IC and in the southern and central GIN Seas (Fig.
222 4c). In the southern hemisphere, partial cells have a more pronounced effect, leading to a significant, up to
223 1000 m, decrease in MLD in the central Weddell Sea (WS) and a minor increase in MLD of around 300 m
224 along the eastern continental slope of the Antarctic Peninsula.

225 The differences between using full cells and partial cells in Global-, Atlantic- and Indo-Pacific Overturning
226 Circulation (Fig. 5) are rather small with magnitudes of less than 1Sv. Both cases feature an upper AMOC
227 circulation cell of ~ 16 Sv and an Antarctic Bottom Water (AABW) cell with strength between -1 Sv and -2
228 Sv. One can summarize that partial cells lead to an improvement of the circulation pattern, especially
229 regarding the reduced zonality of the Gulf Stream and NAC branch even in rather coarse resolved
230 configurations.

231 **3.2 Embedded sea ice**

232 As described in Scholz et al. (2019), FESOM2.0 supports the full free surface formulation with two possible
233 options, zlevel and zstar (Adcroft and Campin, 2004). Both options allow for surface freshwater exchanges
234 which can modify the thickness of the surface layer and thus decrease or increase salinity in the surface
235 layer. This avoids the need of virtual salinity fluxes, which are required in the linear free surface (linfs)
236 approach when the layer thicknesses are kept fixed. Using virtual salinity fluxes has the potential to affect
237 the model integrity on long timescales and change local salinities with certain biases (Scholz et al., 2019).

238 In reality part of sea ice is embedded in the ocean with impact on the ocean pressure below. In the model,
239 when the sea ice loading is omitted, the “levitating” sea ice (Campin et al., 2008) does not impose pressure
240 on the ocean. This is the default case in the case of linfs but also applicable to zlevel and zstar. The other
241 case when ice-loading is considered has “embedded” sea ice (Rousset et al., 2015), which depresses the sea
242 surface according to its mass. Since it affects the layer thicknesses, this case is only available for the full free
243 surface cases of zlevel and zstar. Although freezing and melting have no direct effect on the oceanic
244 pressure, the divergence of the ice transport does modify the ice-loading fields and influences the hydrostatic
245 pressure (Campin et al., 2008). As mentioned by Campin et al., 2008, this effect could be compensated by
246 the divergence of the oceanic transport in the special case where sea ice and ocean velocities match, but in
247 reality sea ice and ocean velocities are not identical especially in the presence of high frequency wind
248 forcing. Therefore, sea ice dynamics in combination with the ice-loading coupling can be a source of oceanic
249 variability especially near the ice-edge where ice divergence/convergence is large (Campin et al., 2008).

250 However, using embedded sea ice harbours the risk that the amount of sea ice loading due to excessive
251 accumulation and the resulting depression in the surface elevation may result in a depletion of the surface
252 layer thickness, when the zlevel option is used, where only the surface layer is allowed to change. To avoid
253 this issue, we limit in FESOM2.0 the maximum ice loading to a sea ice height of 5m when the zlevel option
254 is used. In case of using zstar, the problem is less severe, since here the change in elevation is distributed
255 over all vertical layers, except for the bottom one. This makes zstar to be the recommended option when
256 using embedded sea ice, as also stated by Campin et al., 2008.

257 To show the effect of embedded sea ice on the simulated ocean state, two simulations were carried out using
258 the zstar option of FESOM2.0, one with levitating (omitting the effect of sea ice loading on ocean pressure)
259 the other with embedded sea ice (including the effect of sea ice loading on ocean pressure).

260 Fig. 6 shows the sea ice concentration (SIC) for March and September in the levitating sea ice case and the
261 difference between the embedded and levitating sea ice cases. Superimposed are the simulated (solid) and
262 observed (dashed, Cavalieri et al., 1996) contour line of the 15% sea ice extent. The northern hemispheric
263 March sea ice edge (Fig. 6a) shows a good agreement with observational data for the LS, IS and Bering Sea
264 but reveals a too far southwards extension in the Greenland Sea and Barents Sea. The simulated northern
265 hemispheric (September) sea ice extent (Fig. 6b) is larger than the observations. The southern hemispheric
266 (March) sea ice extent is underestimated in the simulation, while the simulated southern hemispheric
267 (September) sea ice extent is in good agreement with the observation.

268 Using the embedded sea ice leads to an increase in the SIC in the Greenland Sea by around 6% in March. In
269 September, embedded sea ice leads to positive SIC anomalies in the eastern- and negative anomalies in the
270 western AO. In the southern hemisphere, embedded sea ice leads to a heterogeneous pattern of small positive
271 and negative changes along the sea ice edge. The corresponding results for the sea ice thickness are shown in
272 Suppl. 4, here both March and September northern hemisphere sea ice thickness anomalies reveal a dipole
273 like pattern with reduced sea ice thickness in the area of the Beaufort gyre and increased sea ice thickness in
274 the eastern AO and region of the transpolar drift when using embedded sea ice.

275 Regarding the changes in the ocean, Fig. 7 shows the temperature (left column) and salinity (right column)
276 differences between the embedded and levitating (embedded minus levitating) sea ice cases averaged over
277 the depth ranges 0-250 m, 250-500 m, 500-1000 m, 1000-2000 m and 2000-4000 m. The temperature and
278 salinity differences reveal that a significant warming of up to 0.5°C and a salinification of up to 0.10 psu
279 occurs in almost the entire AO due to embedded sea ice, except in a thin stripe along the eastern continental
280 shelf of the AO that shows negative anomalies in the depth ranges of 0-250 m, 250-500 m and 500-1000 m.

281 The changes in temperature and salinity can be explained by the changes in ocean currents. Figure 8 depicts
282 the speed of the horizontal currents in levitating (1st column) and embedded (2nd column) sea ice cases as
283 well as their difference (3rd column). Using embedded sea ice leads to an increase in the speed along the
284 entire boundary current of the Eurasian Basin and along the Lomonosov Ridge, that can be found in all three
285 presented depth ranges. The increase in the velocity of the boundary currents, caused by using embedded sea

ice, leads to an enhanced heat and salt transport in the Atlantic water layer originating from the Fram Strait, which results in a warmer and more saline intermediate depth in the Arctic Ocean (Suppl. 5). The increase in temperature and salinity, especially in the surface layers of the AO using embedded sea ice reduces existing local biases (see Fig. 1 and Fig. 2) that occur when using levitating sea ice. On the whole it can be stated that using embedded sea ice instead of levitating sea ice has some significant effect on the ocean dynamics of the AO, but no effect in the Southern Ocean or Antarctic marginal seas.

3.3 Implementation and evaluation of vertical mixing schemes

Besides the already existing Pacanowski and Philander (fesom_PP, Pacanowski and Philander, 1981) and MOM4 K-profile (fesom_KPP, Large et al., 1994) vertical mixing parameterizations in FESOM2.0 that were based on the implementation in the predecessor version FESOM1.4, the vertical mixing parameterizations of the Community Vertical Mixing (CVMix, Griffies et al., 2015) project have been now added as well. This includes the CVMix vertical mixing of: Pacanowski and Philander (cvmix_PP), the POP (Parallel Ocean Program) K-profile (cvmix_KPP) parameterization, the tidal mixing parameterization of Simmons et al., (2004) (cvmix_TIDAL) and the turbulent kinetic energy (cvmix_TKE) mixing of (Gaspar et al., 1990) in combination with the Internal Wave Dissipation, Energy and Mixing (IDEMIX) parameterization (Olbers and Eden, 2013 and Eden and Olbers, 2014). Although cvmix_TKE and IDEMIX are not yet a part of the CVMix project, they use its libraries in the background and will join the project in the future. CVMix is used by a variety of models, such as MOM6, POP, MPAS or ICON and provides an opportunity of a cross model-spanning vertical mixing implementation that allows for an enhanced cross-model intercomparison.

3.3.1 Comparison of cvmix_KPP, cvmix_PP with previous fesom_KPP and fesom_PP implementation

In FESOM2.0 we implemented cvmix_PP and cvmix_KPP in addition to its previous implementations fesom_PP and fesom_KPP that were adopted from FESOM1.4. The difference between cvmix_PP and fesom_PP lies in the background coefficient for viscosity which is considered in cvmix_PP but not in fesom_PP when computing the diffusivity, following the experience with FESOM1.4 which did not need to be more diffusive. The difference between cvmix_KPP and fesom_KPP lies mainly in the treatment of the squared velocity shear and buoyancy difference with respect to the surface, although CVMix does not make any specific requirements here. In cvmix_KPP we synchronized the implementation with our project partner models MPIOM and ICON-o and compute the cvmix_KPP surface quantities by averaging over 10% of the boundary layer depth as recommended by Griffies et al. 2015 while in fesom_KPP the surface values are linked to the first layer in the model which was inspired by the implementation in the older MOM4.

Suppl. 6 displays the temperature (1st and 2nd column) and salinity (3rd and 4th column) biases of fesom_KPP with respect to WOA18 (1st and 3rd column) as well as the difference between fesom_PP and fesom_KPP (2nd and 4th column). In the surface depth range the climatological temperature and salinity biases of fesom_KPP

321 with respect to WOA18 are largely negative in the tropical and subtropical Pacific, North and South Atlantic
 322 as well as AO, and positive in tropical Atlantic and Indian Ocean, Southern Ocean, Labrador Sea, GIN Seas
 323 and the marginal seas of the North Pacific. The subsurface depth ranges of 250-500 m and 500-1000 m are
 324 dominated by largely positive temperature biases, except for the Southern Ocean, the pathway of the GS and
 325 NAC and the northern Indian Ocean. The salinity biases in the 250-500 m and 500-1000 m depth range
 326 preserve largely the pattern from the surface layer except for an increasing and expanding positive salinity
 327 bias in the tropical Atlantic, reduced positive salinity biases in the Indian Ocean and northern Pacific as well
 328 as reduced negative biases in the Arctic Ocean. The 1000-2000 m depth range features small warm biases in
 329 the AO and GIN seas, positive temperature and salinity biases in the LS and the South Atlantic, negative
 330 temperature and salinity biases in the eastern North Atlantic (possibly due to weak mediterranean outflow)
 331 and small negative temperature and salinity biases in the Pacific and Indian Ocean. The very deep depth
 332 range of 2000-4000 m reveals rather small warming bias for the entire Atlantic and SO.

333 fesom_KPP and fesom_PP produced rather small temperature and salinity differences (note different
 334 colorbar ranges between 1st & 2nd and 3rd & 4th column), considering the biases with respect to the WOA18
 335 climatology. Employing fesom_PP has the tendency to be slightly warmer almost everywhere in the
 336 subsurface layers and slightly saltier especially in the AO and fresher in the surface layer of the subtropical
 337 and equatorial ocean compared to using fesom_KPP. Looking at the maximum MLD between fesom_PP and
 338 fesom_KPP (Suppl. 7) it can be seen that fesom_PP has the tendency to produce an up to 500m shallower
 339 deep convection in LS and WS when compared to fesom_KPP.

340 Fig. 9 shows the difference in temperature (1st column), salinity (2nd column) and vertical diffusivity (3rd
 341 column) between cvmix_KPP and fesom_KPP (cvmix_KPP minus fesom_KPP) averaged over five different
 342 depth ranges. The last column presents the fesom_KPP vertical diffusivity as a reference. Also here, the
 343 temperature and salinity differences are rather small compared to the climatological biases shown in Suppl.
 344 6. cvmix_KPP has the tendency to produce in the marginal seas of the AO a slightly fresher surface ocean,
 345 while the central AO shows an increase in salinity by ~ 0.1 psu.

346 The absolute value of the vertical diffusivity in fesom_KPP is larger than that in cvmix_KPP in the surface
 347 layers as well as in regions of unstable stratification (buoyancy frequency < 0), superimposed on a non-
 348 constant background diffusivity as described in Scholz et al., 2019. The different treatment of the squared
 349 velocity shear and buoyancy difference with respect to the surface in cvmix_KPP leads to a reduction of the
 350 vertical diffusivity (3rd column) in the Labrador and Irminger Seas and to an increase in the AO locally by up
 351 to one order of magnitude (especially in the deep ocean).

352 The differences in MLD between fesom_KPP and cvmix_KPP are presented in Fig. 10, where a) and b)
 353 show the absolute MLD value for fesom_KPP in the northern hemisphere in March and in the southern
 354 hemisphere in September respectively. Fig. 10 c) and d) display the corresponding anomalies between
 355 cvmix_KPP and fesom_KPP (cvmix_KPP-fesom_KPP). The absolute MLD values for fesom_KPP in March
 356 show high values of up to 3300 m in the entire LS and parts of the Irminger Sea, intermediate values of up to

2000 m in the northern and eastern GIN seas and values of ~900m along the eastern continental slope of the North Atlantic. In the southern hemisphere in September, fesom_KPP simulates a large MLD of ~2500 m in the central Weddell Sea and weaker MLD of ~500 m in the band of the Antarctic Circumpolar Current (ACC). Compared to the fesom_KPP, cvmix_KPP leads to a ~200 m weaker MLD in the boundary currents of the LS, southern LS and along the northeastern continental slope of the GIN seas, and slightly larger MLD values in the IS and southwestern GIN Seas. The KPP ocean boundary layer depth (OBLd, Large et al. 1994) for fesom_KPP and the difference in OBLd between cvmix_KPP and fesom_KPP is additionally presented in Suppl. 8, where it is shown that cvmix_KPP produces a around 150 m shallower OBLd which is largely attributed to the different treatment of the surface quantities by averaging over 10% of the boundary layer depth.

Fig. 11 presents the differences in temperature (1st column), salinity (2nd column) and vertical diffusivity K_v (3rd column) between cvmix_PP and fesom_PP (cvmix_PP minus fesom_PP) as well as the absolute values of vertical diffusivity for fesom_PP (4th column). For the upper two surface depth ranges, cvmix_PP shows an overall small warming anomaly, except for the Gulf of Guinea in the 250-500 m depth range where the anomaly is negative. The salinity with cvmix_PP has overall slight positive anomalies, except for coastal Arctic areas and the Gulf of Guinea which indicate a slight freshening anomaly when compared to fesom_PP. The depth ranges below 500 m show no significant temperature or salinity differences between cvmix_PP and fesom_PP. The absolute value of K_v in fesom_PP also shows larger values all over the surface layer as well as in the areas of unstable stratification similar to fesom_KPP, but with a lower magnitude and a more extended region of increased K_v in the LS and IS. The K_v difference between cvmix_PP and fesom_PP shows sporadically positive values along the coastal Arctic Ocean and in parts of the North Atlantic and GIN Seas. As one would expect, cvmix_PP has an order of magnitude larger values in the very deep ocean layer where the background viscosity enters the computation of K_v in cvmix_PP.

Fig. 12 presents the absolute and anomalous MLD between fesom_PP and cvmix_PP. The MLD in fesom_PP in March is deep in the entire LS and in parts of the IS, but slightly weaker and less spatially extended when compared to fesom_KPP (Fig. 10). The MLD in the GIN seas is very similar between fesom_PP and fesom_KPP. In the southern hemisphere the September MLD in fesom_PP shows a pattern in the central Weddell Sea which is similar to that in fesom_KPP, but shallower by ~500 m. The MLD difference between cvmix_PP and fesom_PP in the northern hemisphere indicates a very heterogeneous pattern for the North Atlantic and in the southern hemisphere an up to ~150 m deeper MLD in the Weddell Sea MLD for cvmix_PP compared to fesom_PP. Overall, the difference in the simulation results induced by the difference in the two implementations of mixing schemes is generally small when considering the model biases relative to observations.

3.3.2 Effects of tidal mixing parameterization of Simmons et al. (2004)

The tidal mixing parameterization of Simmons et al., (2004) provided by CVMix has been added to FESOM2.0. This mixing parameterization takes into account effects from internal wave generation due to

393 tides over rough bottom topography. The breaking of internal waves in the vicinity of topographic features
 394 excites small-scale turbulence and leads to an enhanced vertical mixing. The tidal mixing parameterization
 395 uses a two dimensional map of tidal energy dissipation flux due to bottom drag and energy conversion into
 396 internal waves from Jayne and St. Laurent, (2001). It is transformed under consideration of a vertical
 397 redistribution function, the modelled buoyancy frequency and a tidal dissipation efficiency and mixing
 398 efficiency into a 3D map of diapycnal tidal vertical mixing, which is added to a primary vertical mixing
 399 scheme like PP, KPP or TKE. To show the effect of the tidal mixing parameterization we conducted a
 400 simulation using both `cvmix_KPP` and the tidal vertical mixing (`cvmix_KPPTIDAL`). This simulation will be
 401 compared with a control run with `cvmix_KPP` in which the tidal mixing is not considered. The differences in
 402 temperature (1st column), salinity (2nd column) and vertical diffusivity K_v (3rd column) between
 403 `cvmix_KPPTIDAL` and `cvmix_KPP` averaged over five different depth ranges are presented in Fig. 13. The last
 404 column of Fig. 13 shows the `cvmix_KPP` K_v as a reference. The temperature anomalies of the upper three
 405 depth ranges indicate that `cvmix_KPPTIDAL` is colder especially in the marginal seas of the North Pacific, e.g.
 406 Sea of Japan, Sea of Okhotsk and Bering Sea, within the branch of the Gulf Stream (GS) and North Atlantic
 407 Current (NAC) as well as in the GIN- and Barents Seas. The Arctic Ocean shows a cooling anomaly for the
 408 500-1000 m and 1000-2000 m depth range. In the southern hemisphere the entire Southern Ocean is slightly
 409 colder when including the tidal vertical mixing. The tropical and subtropical ocean indicates a slight
 410 warming for `cvmix_KPPTIDAL`.

411 The salinity anomalies between `cvmix_KPPTIDAL` and `cvmix_KPP` show a pattern similar to that of the
 412 temperature, with a freshening in the marginal seas of the North Pacific, GS, NAC, GIN- and Barents Seas as
 413 well as for the Southern Ocean. The upper depth range indicates an increase in salinity for the AO, while the
 414 subsurface depth ranges show an AO freshening when including the tidal mixing. The tropical and
 415 subtropical ocean shows largely an increase in salinity under `cvmix_KPPTIDAL`.

416 The difference in vertical diffusivity shows for `cvmix_KPPTIDAL` an increase by an order of magnitude along
 417 the sloping bottom topography (e.g. the Midatlantic Ridge or Indonesian region) but also along the
 418 continental shelf regions which is induced by the tidal vertical mixing parameterization. On top of that the
 419 central AO shows a reduced vertical diffusivity by at least an order of magnitude for the 250-500 m, 500-
 420 1000 m and 1000-2000 m depth ranges, which comes from a change in local hydrography when including
 421 the tidal vertical mixing parameterization and the associated difference in the KPP mixing scheme.

422 To further understand the effect of the tidal vertical mixing, Fig. 14 shows the global zonal mean temperature
 423 and salinity differences between the case of `cvmix_KPP` and the WOA18 (a, c) and the differences between
 424 `cvmix_KPPTIDAL` and `cvmix_KPP` (b, d). The temperature of `cvmix_KPP` shows a rather strong warming bias
 425 until 1000 m for the tropical and subtropical ocean as well as until ~2500 m for the ocean north of 50°N with
 426 respect to WOA18 (Fig. 14a). The deep ocean features small negative temperature anomalies for the tropical
 427 and subtropical ocean and slightly positive biases for the deep SO, when compared to WOA18. The salinity
 428 biases of the `cvmix_KPP` case (Fig. 14c) indicate a more heterogeneous but nevertheless similar picture.

429 Also here positive salinity biases can be seen in the tropical and subtropical ocean until around 1000m as
 430 well as until ~2500m for the ocean north of 50°N. Looking at the temperature and salinity difference
 431 between `cvmix_KPPTIDAL` and `cvmix_KPP`, it can be seen that the tidal mixing of Simmons et al.,
 432 (2004) leads to a cooling and freshening of the Southern Ocean and the ocean north of 50°N as well as a
 433 warming and salinification for the tropical and subtropical ocean until around 1500m. The deep ocean
 434 experiences a general slight warming and freshening due to the inclusion of the tidal mixing
 435 parameterization. In general one can summarize that the tidal mixing parameterization of Simmons et al.,
 436 (2004) helps to improve some of the biases with respect to WOA18. The last panel in Fig 14e shows the
 437 global zonal averaged vertical diffusivity profiles between `cvmix_KPPTIDAL` and `cvmix_KPP` and reveals a
 438 general strong increase in K_v along the continental slope in the southern ocean, in the northern hemisphere
 439 north of 50°N as well as in the deep ocean interior.

440 To illustrate the effect of Simmons et al., (2004) tidal mixing parameterization onto the MLD, Fig. 15
 441 presents the northern hemisphere (March) (a) and southern hemisphere (September) (b) MLD in the case of
 442 `cvmix_KPP`, and the difference in MLD between `cvmix_KPPTIDAL` and `cvmix_KPP` also for northern
 443 hemisphere (March) (c) and southern hemisphere (September) (d). In the northern hemisphere in March,
 444 tidal mixing leads to an increase in the MLD within the boundary currents of the LS, southern and eastern
 445 GIN Seas as well as in the Sea of Okhotsk. In the southern hemisphere (September), tidal mixing leads to a
 446 significant ~1000 m increase in the Weddell Sea MLD. This significant increase originates largely from
 447 enhanced mixing of very cold surface waters along the continental slope of the Weddell Sea due to the tidal
 448 mixing parameterization. Suppl. 9 shows the KPP OBLd for `cvmix_KPP` and the difference in OBLd
 449 between `cvmix_KPP` with and without the tidal mixing of Simmons et al., (2004). It shows that with
 450 `cvmix_KPPTIDAL` the OBLd deepens especially in the western LS.

451

452 3.3.3 Effects of Turbulent-Kinetic-Energy (TKE) mixing parameterisation

453 More elaborate parameterizations of the vertical mixing in the ocean can be achieved by using closure
 454 schemes of turbulent kinetic energy (TKE) and the associated turbulent mixing within the mixed layer and
 455 below. One of these turbulent closure schemes is by Gaspar et al. (1990) that has been implemented via
 456 `CVMix (cvmix_TKE)` into FESOM2.0 based on the work of Eden et al. (2014) and Gutjahr et al. (2020). The
 457 turbulence closure scheme requires the solving of the second-order equation for TKE which is closed by
 458 connecting the vertical diffusivity with the turbulent kinetic energy and a length scale for its dissipation
 459 (Eden et al., 2014). For the background diffusivity we do not use the latitude and depth dependent
 460 background diffusivity as in the previous mixing schemes. Instead, a constant minimum value of TKE is
 461 assumed, which takes into account the ocean interior mixing by internal wave breaking. To understand the
 462 effect of `cvmix_TKE` on oceanic hydrography, Fig. 16 presents the temperature and salinity biases of
 463 `cvmix_TKE` with respect to WOA18 (1st and 3rd column). To relate `cvmix_TKE` to the other vertical mixing
 464 schemes (e.g. KPP), the temperature and salinity differences between `fesom_KPP` and `cvmix_TKE` (2nd and

465 4th column) are shown as well. In general, the cvmix_TKE temperature and salinity biases with respect to
466 WOA18 look largely very similar to the biases of fesom_KPP shown in Supp2. 1 (1st and 3rd column) in
467 terms of the spatial patterns. A closer inspection of temperature and salinity differences between cvmix_TKE
468 and fesom_KPP (Fig. 16, 2nd and 4th column) reveals that cvmix_TKE produces an up to 0.5°C colder ocean
469 within the 0-250 m, 250-500 m and 500-1000 m depth ranges in most of the ocean, a strong warming along
470 the pathway of the NAC and the southern polar front in the South Atlantic, and small warming biases in the
471 AO and SO. The salinity differences between cvmix_TKE and fesom_KPP indicate a salinification of the
472 AO throughout the 0-250 m, 250-500 m and 500-1000 m depth ranges, but most pronounced in the surface
473 depth range. The surface saline bias largely stems from reduced mixing under sea ice, which shields the
474 ocean from the wind stress, a large source term of TKE. Furthermore, there are positive salinity anomalies in
475 the North Atlantic (in the pathway of the GS and NAC), North Pacific and Southern Ocean, and largely
476 negative salinity anomalies in the southern hemisphere. The temperature and salinity differences between
477 cvmix_TKE and fesom_KPP in the depth ranges of 1000-2000 m and 2000-4000 m are rather marginal. It
478 should be mentioned that a part of the anomalies described here could also be attributed to the different
479 treatment of the background diffusivity. fesom_KPP takes a latitude and depth dependent value (Scholz et
480 al., 2019), while cvmix_TKE assumes a constant value of minimum TKE on the surface ($10e-4 \text{ m}^2/\text{s}^2$) and
481 for the interior mixing ($10e-6 \text{ m}^2/\text{s}^2$).

482 **3.3.4 Effects of energy consistent combination of TKE with the Internal Wave Dissipation** 483 **Energy and Mixing (IDEMIX) parameterisation**

484 Besides the standard implementation of vertical background diffusivity in cvmix_TKE using a constant
485 minimum value of TKE to parameterize the effect of breaking of internal waves, cvmix_TKE also allows for
486 the usage of a more sophisticated parameterization of internal wave breaking when combined with the
487 IDEMIX parameterization (Olbers and Eden, 2013; Eden et al., 2014) which describes the energy transfer
488 from sources towards sinks of internal waves by using a radiative transfer equation of weakly interacting
489 internal waves. The resulting dissipation of energy is then treated as a source term in the turbulent kinetic
490 energy balance equation leading at the end to an energetically more consistent interpretation of the internal
491 ocean mixing process (Eden et al., 2014; Gutjahr et al., 2020). Thereby, IDEMIX solves for the propagation
492 of low-mode internal waves far from their generation sites, which is considered by Fox-Kemper et al., (2019)
493 as one of the most difficult components of the internal wave energy budget. Different from the tidal mixing
494 parameterization of Simmons et al., (2004), which only represents the generation of internal waves by
495 barotropic tides and their breaking at rough topography, IDEMIX considers both the internal waves due to
496 barotropic tides and the internal waves induced by wind-stress fluctuations and exiting at the base of the
497 mixed layer (Gutjahr et al., 2020). The combination of cvmix_TKE and IDEMIX to improve the energetic
498 consistency of ocean models is a rather new approach in the modelling community. It has been evaluated for
499 stand-alone ocean models (Eden et al., 2014; Nielsen et al., 2018; Pollmann et al., 2017) and coupled models
500 (Nielsen et al., 2019). Further, the computed TKE dissipations rates from IDEMIX have been evaluated

501 against observational Argo float-derived dissipation rates by Pollmann et al. (2017) and have been found to
 502 be in good agreement (Gutjahr et al., 2019). In this part of the FESOM2 documentation, two FESOM2.0
 503 simulations with `cvmix_TKE`, one with and one without the usage of IDEMIX, are compared to assess the
 504 effect of IDEMIX on the modelled hydrography.

505 Fig. 17 presents the temperature (1st column), salinity (2nd column) and vertical diffusivity (3rd column)
 506 differences between `cvmix_TKE` with IDEMIX versus without it, averaged over five different depth layer
 507 ranges. As a reference the vertical diffusivity of `cvmix_TKE` without IDEMIX is also shown in the 4th
 508 column. The temperature differences indicate a clear warming of all equatorial and mid-litudinal oceans
 509 and a cooling in the AO, SO and the marginal seas of the North Pacific throughout almost all the depth
 510 ranges, when `cvmix_TKE` is used with IDEMIX. There is a particularly strong warming in the surface and
 511 subsurface depth range of the North Atlantic, in the subsurface depth range of the south Pacific and in the
 512 deeper depth ranges of the Indian Ocean. The salinity differences (2nd column) have a similar spatial pattern,
 513 showing a rather strong salinification of the equatorial and mid-litudinal global oceans and a freshening of
 514 the AO, SO and North Pacific from the surface to 500-1000 m depth range. The depth ranges below indicate
 515 a predominant general freshening almost everywhere, except for the Mediterranean outflow and Indian
 516 Ocean which indicate a slight salinification. The differences in the vertical diffusivity between `cvmix_TKE`
 517 with and without IDEMIX are only very small in the upper layer depth range. Therefore, all subsurface depth
 518 layers indicate considerable positive vertical diffusivity differences by up to two orders of magnitude
 519 especially along all major topographic features as well as in the SO. This shows in particular how IDEMIX
 520 parameterizes the vertical mixing due to the breaking of upwards propagating internal wave excited by
 521 barotropic tides along the ocean bottom topography but also the vertical mixing related to the internal wave
 522 breaking of downward propagating internal waves radiated out of the mixed layer like e.g. in the SO.

523 Fig. 18 presents the global zonal mean temperature and salinity differences of `cvmix_TKE` with respect to
 524 the WOA18 (a, c) as well as the temperature, salinity and vertical diffusivity differences between
 525 `cvmix_TKEIDEMIX` and `cvmix_TKE` (b, d, e). The zonal mean temperature biases of `cvmix_TKE` with respect
 526 to WOA18 (Fig. 18a) are positive for the upper SO, the equatorial and mid-litudinal oceans between 500m
 527 until 1000m, and the high-latitude ocean north of 60°N where the warming bias extends nearly from the
 528 surface until a depth of ~2500m. A rather weak warming bias is also present for the very deep >2500m SO.
 529 General cooling biases can be seen for the equatorial and mid-litudinal surface oceans, between a depth of
 530 ~1000m to 2000m as well as for the very deep ocean. The salinity biases for `cvmix_TKE` (Fig. 18c) show too
 531 high salinities for the high-latitude ocean north of 40°N and for the surface SO. Small salinity biases can be
 532 found in the equatorial and mid-litudinal surface layers as well as around 40°N between ~1000 and 3000
 533 m.

534 The temperature differences between `cvmix_TKE` with and without IDEMIX (Fig. 18b) shows that the
 535 IDEMIX leads to a general warming of the equatorial and mid-litudinal oceans especially between ~500 m
 536 and ~2000 m, but a cooling in the northern and southern high-latitude oceans. The salinity differences

537 between `cvmix_TKE` with and without IDEMIX reveal a similar pattern with an increase in salinity for the
 538 equatorial and mid-latitude ocean from the surface until a depth ~ 2000 m and a freshening bias in the same
 539 depth range for the high-latitude oceans and for the entire deep ocean as well.

540 The corresponding vertical diffusivity difference is shown in Fig. 18e. There, using IDEMIX results in an
 541 increase in vertical diffusivity along the bottom topographic slopes in the SO and north of 50°N until 70°N .
 542 Further, an increase in vertical diffusivity can be observed for almost the entire upper ocean until ~ 2000 m
 543 with deeper reaching positive anomalies between $-60^\circ\text{S} - 30^\circ\text{S}$ and $30^\circ\text{N} - 50^\circ\text{N}$. A reduction of the vertical
 544 diffusivity can be observed for the entire AO from the surface to bottom, for the equatorial and mid-
 545 latitude deep ocean >3000 m as well as for the deep (>4000 m) SO.

546 The effect of IDEMIX on the MLD is presented in Fig. 19, which shows the northern hemisphere (March) a)
 547 and southern hemisphere (September) b) `cvmix_TKE` MLD and the corresponding anomalies between
 548 `cvmix_TKE` with and without IDEMIX. It indicates that the use of IDEMIX leads to an increase in northern
 549 hemisphere MLD within the boundary currents of the LS by up to ~ 1000 m and in the southeastern GIN Seas
 550 by up to ~ 1800 m. In the southern hemisphere (September), IDEMIX leads to a significant increase of the
 551 Weddell Sea MLD up to ~ 1800 m. We observe that using `cvmix_KPPTIDAL` or `cvmix_TKEIDEMIX` the model
 552 cannot maintain the upper halocline in the Weddell Sea. Hence the warm water that shall stay deep is
 553 exposed to the surface and the ocean loses heat. It can be well seen from Fig. 14.b and 18.b as blobs of
 554 negative temperature differences beneath the surface. As a consequence, the enlarged MLDs in the Weddell
 555 Sea appear. We therefore recommend to combine `cvmix_KPPTIDAL` or `cvmix_TKEIDEMIX` with the partial
 556 bottom cell approach, which has a partly compensating effect on the stratification in the Weddell Sea (see
 557 section 3.1 and Suppl. 3) and leads to a reduction of the MLD (Suppl. 10) due to improvements of the current
 558 circulation in the Weddell Sea.

559 **3.4 Implementation of Monin-Obukhov length dependent vertical mixing**

560 In this section the effect of the Monin-Obukhov length vertical mixing (MOMIX) of Timmermann and
 561 Beckmann (2004) in FESOM2.0 is discussed. In an attempt to decrease the climatological biases especially
 562 in the Southern Ocean, which were otherwise prone to significant cooling and salinification (not shown),
 563 MOMIX has been implemented into FESOM2.0 as well. MOMIX serves as a parameterisation of the wind
 564 driven mixing in the Southern Ocean, effective especially in the melting season, which helps to reduce
 565 winter deep convection in the Weddell Sea, thus affecting the basin wide ocean- and meridional overturning
 566 circulation (Timmermann and Beckmann, 2004). MOMIX computes the Monin-Obukhov length based on
 567 heat flux, freshwater flux, wind stress, sea ice concentration and sea ice velocity following the approach of
 568 Lemke (1987), and subsequently increases the vertical diffusivity within the Monin-Obukhov length to a
 569 value of $0.01\text{m}^2/\text{s}$.

570 Due to its success in reducing the aforementioned mean biases, MOMIX is applied at the moment in
 571 FESOM2.0 per default south of -50°S . In the following, the effects of MOMIX are discussed, based on

572 simulation of fesom_KPP and cvmix_TKE each with and without MOMIX.

573 Fig. 20 presents the temperature (1st and 2nd column) and salinity (3rd and 4th column) differences between
 574 simulations with and without MOMIX for both the fesom_KPP and cvmix_TKE schemes, averaged over
 575 five different depth ranges. Using MOMIX in the Southern Ocean leads to a significant warming of up to
 576 1°C for almost the entire Southern Ocean south of -60°S throughout all considered depth ranges, except for
 577 the surface depth range of the southern Weddell Sea and subsurface southern Pacific which exhibits cooling
 578 anomalies. The warming anomaly is slightly more pronounced for fesom_KPP than cvmix_TKE. The usage
 579 of MOMIX in the Southern Ocean leads in fesom_KPP to a warming of the Gulf Stream and to a cooling of
 580 the NAC. For cvmix_TKE this behaviour is reversed. The salinity anomalies indicate a freshening for the
 581 entire Southern Ocean surface depth range when using MOMIX, while the subsurface depth ranges indicate
 582 predominantly a slight increase in salinity, except for the southern Weddell Sea 250-500m depth range.

583 To emphasize the effect of MOMIX on the Weddell Sea MLD, Fig. 21 presents the Southern Ocean
 584 September MLD for fesom_KPP (a) and cvmix_TIDAL (b) without MOMIX and the corresponding
 585 anomalies with minus without MOMIX (c, d). The MLD for fesom_KPP (a) and cvmix_TKE (b) are very
 586 large over the entire Weddell Sea and parts of the Ross Sea. The MLD values are higher and more extended
 587 with fesom_KPP than with cvmix_TKE. However, for both vertical mixing schemes without using MOMIX,
 588 the MLD values are way too high within the Weddell Sea and Ross Sea. The figures c) and d) visualize what
 589 happens with the Southern Ocean MLD for fesom_KPP and cvmix_TKE when MOMIX is used. Especially
 590 for fesom_KPP, MOMIX leads to a significant decrease in the MLD in almost the entire Weddell Sea of up
 591 to ~3000 m, except for the southwestern Weddell Sea close to the continental shelf which exhibits an
 592 increase in MLD. Also the large MLD patch in the Ross Sea becomes strongly reduced when using MOMIX.
 593 Both fesom_KPP and cvmix_TKE face the same pattern in MLD reduction when using MOMIX, only the
 594 magnitude in the MLD decrease is larger in fesom_KPP than in cvmix_TKE.

595 Since MOMIX has a rather strong effect in reducing the Weddell Sea open-ocean deep-water formation it
 596 will also consequently affect the formation of Antarctic Bottom Water (AABW) and the Meridional
 597 Overturning Circulation (MOC). Fig. 22 shows the fesom_KPP global (a), Atlantic (b) and Pacific (c) MOC
 598 when MOMIX is switched off and the difference from the case with MOMIX (bottom row). It can be seen
 599 that on a global but also basin-wide scale, the use of MOMIX leads to a reduction in the strength of the
 600 AABW, in the Atlantic by ~0.6 Sv and in the Pacific by up to ~1.7 Sv. Also the strength of the upper AMOC
 601 cell is reduced by ~1 Sv when using MOMIX. We conclude that using MOMIX helps to alleviate the
 602 problem of large MLDs in the Weddell Sea which we addressed above. Hence, the options cvmix_KPP_{TIDAL}
 603 or cvmix_TKE_{IDEMIX} are strongly recommended to be used in combination with MOMIX, which is per
 604 default active only South of -50°S.

605

606 4 Discussion and Conclusions

607 This paper describes the two new features -- partial cells and embedded sea ice introduced to FESOM2.0 and
608 the implementation of the vertical mixing library CVMix (cvmix_PP, cvmix_KPP, cvmix_TKE, IDEMIX
609 and cvmix_TIDAL), together with the elaboration of the effect of MOMIX. These new features expand the
610 functionality of FESOM2.0, its applicability and its ability to be better compared to other state of the art
611 ocean general circulation models. With its model components implemented, FESOM2.0 is mature for its
612 practical applications and holds its leading role in the competition of the global unstructured ocean models.

613 We demonstrate the effect of using partial cells by comparing them against the full cell approach. It is shown
614 that partial cells lead to an improved representation of the Gulf Stream branch, with a reduction in the cold
615 bias in the northwest corner of the North Atlantic associated with an improved NAC pathway. Further,
616 partial cells lead to a “northwest corner like” meridional deflection of the NAC between -30°W and -15°W
617 which is still too far east, but leads to an improved representation in a rather coarse configuration which
618 would otherwise be dominated by a rather zonal NAC. Partial cells also lead to a general speed up of the
619 boundary currents shown as an example for the North Atlantic.

620 The improvement of the NAC pathway and the speedup of the boundary currents especially in the subpolar
621 gyre by using partial cells is described by a variety of publications (e.g. Barnier et al., 2006; Käse et al.,
622 2001; Myers, 2002). Besides all its advantages, partial cells also harbor the risk of increasing the existing
623 biases, like in our coarse configuration the deep Arctic warm bias, which is largely inherited from the
624 Atlantic Water inflow branch that expands too deep. The tendency of partial cells to increase the velocity in
625 the boundary currents leads to an enhancement of the Atlantic Water inflow to the Arctic Ocean. As the
626 temperature in the Arctic Atlantic Water layer is already overestimated without using partial cells, the warm
627 bias becomes even larger when partial cells are used. However, this is not the principle drawback of partial
628 cells, but rather an issue of model tuning for the pan-Arctic region, which is part of our on-going work (for
629 example, evaluating different numerical schemes of momentum viscosity). In the southern hemisphere, using
630 partial cells leads to a significant reduction of the otherwise rather high MLD in the Weddell Sea. Regarding
631 the configuration used in this paper, using partial cells leads to a strengthening of the warm deep water
632 current (Vernet et al. 2019) that crosses the Weddell Sea interior. Thus it enhances the local stratification
633 (see Suppl. 3 white arrow) and reduces vertical convection. It can be summarized that the usage of partial
634 cells clearly improves the general circulation within FESOM2.0 and that the benefits outweigh the
635 drawbacks.

636

637 The second feature that was presented, is the effect of embedded sea ice vs. the standard case of levitating
638 sea ice. Embedded sea ice allows for a further step towards a more realistic and physical ocean-sea ice
639 interaction by adding the sea ice loading to the ocean pressure. This has the potential of increasing ocean
640 variability especially near the sea ice edge. Our results indicate that the embedded sea ice has only a minor

641 effect on the sea ice distribution itself. Nevertheless the effect is the strongest for the Northern Hemisphere
642 summer, when the sea ice edge retracts towards the Arctic Ocean interior. Here embedded sea ice leads to an
643 up to 9% increase in the sea ice concentration in the eastern Arctic Ocean marginal seas, which also leads to
644 an increase in the bias of the sea ice edge, and to a 6% decrease in the marginal seas of the western Arctic
645 Ocean, which slightly reduces the sea ice extent bias there. The effect of embedded sea ice on the
646 hydrography of the Arctic Ocean is much more significant, with an increase in temperature and salinity of up
647 to 0.5°C and 0.1psu, respectively through most of the upper 1000 m. The increase in temperature and salinity
648 is connected to a particular increase of the boundary currents especially along the eastern boundaries of the
649 Eurasian Basin but also to a strengthening of the cyclonic current along the Lomonosov Ridge, which was
650 otherwise rather weakly represented in the levitating sea ice case. The deficiencies of the Arctic Ocean
651 currents representation in our model configuration can be partially attributed to the rather coarse resolution.
652 However, with embedded sea ice we seem to be able to at least partly counteract the effect of low resolution
653 and improve the Arctic Ocean current structure at rather low costs. We note that embedded sea ice could also
654 deteriorate the model results in some cases. Since the boundary currents around the Eurasian Basin get
655 enhanced, the already existing Atlantic Water layer biases get enhanced. However, as mentioned above, this
656 is an issue of model tuning with this coarse resolution setup, not a drawback of embedded sea ice itself.

657

658 To further expand the functionality and comparability of FESOM2.0 we implemented the vertical mixing
659 library CVMix and its components, which in our implementation include `cvmix_PP`, `cvmix_KPP`,
660 `cvmix_TIDAL`, `cvmix_TKE` and `cvmix_TKE+IDEMIX`. At first, the vertical mixing parameterizations
661 `fesom_KPP` and `fesom_PP`, which have been already implemented in FESOM2.0, are briefly evaluated. It is
662 shown that `fesom_PP` produces a slightly colder tropical and subtropical but warmer polar oceans on the
663 surface, with a largely warmer ocean below the surface layer depth range, when compared to `fesom_KPP`.
664 This makes between these two, `fesom_KPP` the preferred vertical mixing option at least in terms of mean
665 temperature biases. In terms of salinity biases, `fesom_PP` performs better in the surface and subsurface AO
666 as well as in the equatorial Atlantic and Indian Ocean, while otherwise `fesom_KPP` indicates smaller biases.
667 In the next instance, `fesom_KPP` and `cvmix_KPP` have been compared to each other, since there are slight
668 differences in their implementation. The difference in implementation leads only to minor differences in
669 temperature throughout all considered depth ranges. Regarding the salinity differences, `cvmix_KPP` produces
670 a considerably fresher surface AO compared to `fesom_KPP`, which is attributed to a reduced near surface
671 vertical diffusivity in `cvmix_KPP` that leads to an over-stabilisation of the AO halocline. This enhances the
672 mean salinity bias in that region. In terms of vertical diffusivity, `cvmix_KPP` has the tendency to produce by
673 up to one order of magnitude lower value (especially in the very deep depth range) in the main convection
674 areas of Labrador Sea and Greenland Sea, throughout all considered depth ranges, accompanied by increased
675 diffusivity in the subsurface of the Arctic Ocean. The reduced diffusivity in the main convection areas is
676 attributed to the different treatment of the shear- and buoyancy difference with respect to the surface in

677 `cvmix_KPP` that leads to a reduction of the local ocean boundary layer depth and to slightly reduced
678 maximum MLD in Labrador and Greenland Sea, while the maximum MLD in the Weddell Sea becomes
679 slightly enhanced, when using `cvmix_KPP` over `fesom_KPP`.

680 Since the implementation of `cvmix_PP` and `fesom_PP` are also slightly different, we also compare them.
681 Although the produced diffusivities between `cvmix_PP` and `fesom_PP` are very similar, `cvmix_PP` indicates
682 a further warming and salinification in the surface and 250-500 m depth ranges except for the upwelling
683 region in the Gulf of Guinea which indicates a cooling and freshening and the surface depth range of the
684 Arctic Ocean where it creates a predominant freshening, when compared the `fesom_PP`. The MLD values
685 indicate that `cvmix_PP` leads in FESOM2.0 to a slightly stronger convection in the Weddell Sea. The
686 differences between `fesom_PP` and `cvmix_PP` are related to the different treatment of the background
687 coefficient for viscosity when computing the diffusivity see Pacanowski and Philander (1981).

688 The effect of implementing `cvmix_TIDAL` in combination with `cvmix_KPP` was further assessed.
689 `cvmix_TIDAL` serves here as a resourceful way to heterogenize the effect of tidally induced internal wave
690 breaking that is otherwise homogenized in a constant or latitude dependent value for the background
691 diffusivity. Using `cvmix_TIDAL` clearly leads to an enhancement of the vertical diffusivity along the slopes
692 of the bottom topography, where tidally related internal wave breaking is induced. This leads especially in
693 the high-latitude marginal seas, e.g. Sea of Okhotsk and Bering Sea but also Arctic Ocean and Southern
694 Ocean, to a decrease in temperature and salinity due to the enhanced mixing along their shelves. This enables
695 `cvmix_TIDAL` to improve some of the existing local temperature and salinity biases within FESOM2.0 at
696 rather low computational costs. However, the enhanced vertical diffusivity along the shelf of the Weddell
697 Sea weakens the stratification and leads to a further increase in the MLD of the Weddell Sea of up to 1000
698 m.

699 Further, the implications of TKE vertical mixing parameterisation in FESOM2.0, added by Eden et al. (2014)
700 and Gutjahr et al. (2020) to the CVMix library, was evaluated based on a comparison with `fesom_KPP`. It is
701 shown that the mean temperature and salinity differences between `cvmix_TKE` (Fig. 17) and `fesom_KPP`
702 (Fig. 9) show very similar patterns. `cvmix_TKE` tends to produce a generally colder tropical and
703 extratropical ocean together with slightly warmer polar oceans when compared to `fesom_KPP`. The salinity
704 differences between `cvmix_TKE` and `fesom_KPP` shows that `cvmix_TKE` tends to produce a significantly
705 saltier surface layer AO, revealing a much smaller salinity bias for the Arctic Ocean interior. This is largely
706 connected to enhanced surface vertical mixing along the Arctic Ocean shelf break (not shown) within
707 `cvmix_TKE`, that helps to partly destabilize the AO halocline. The improvement of the Arctic Ocean
708 hydrography when using `cvmix_TKE` is also found by Gutjahr et al. (2020) in the coupled ocean-atmosphere
709 Max Planck Institute Earth System Model (MPI-ESM1.2). Further, `cvmix_TKE` leads to a salinity increase in
710 the entire North Atlantic and northwest Pacific marginal seas, while the southern hemisphere, except for the
711 Southern Ocean, shows a freshening when compared to `fesom_KPP`. The reduced temperatures and salinities
712 in the tropics and extratropics when using `cvmix_TKE` are connected to the reduced vertical mixing.

713 However the regions of strong vertical shear, e.g. the branch of the Gulf Stream and NAC as well as
714 Southern Ocean show stronger vertical mixing in `cvmix_TKE`, when compared to `fesom_KPP` (not shown),
715 which is accompanied by positive temperature and salinity anomalies between `cvmix_TKE` and `fesom_KPP`.
716 Following the comparison of `cvmix_TKE` and `fesom_KPP`, a side by side comparison of `cvmix_TKE` with
717 and without IDEMIX was carried out. Here IDEMIX provides an alternative formulation of the background
718 diffusivity in `cvmix_TKE` using a radiative transfer equation of weakly interacting internal waves (Olbers
719 and Eden 2013), where energy is transferred from sources of internal waves to wave sinks, such as the
720 breaking of internal waves, which provide a source for TKE, leading to an energetically more consistent
721 treatment of internal mixing (Eden et al. 2014). As compared to the tidal background mixing
722 parameterization of Simmons et al (2004), IDEMIX allows not only for the generation of internal waves by
723 barotropic tides interacting with marine topography, but also for their propagation in the horizontal and
724 vertical directions away from region of generation and their damping due to wave-wave interaction or
725 interaction with the continental shelf. Further, IDEMIX allows for the excitation of internal waves at the base
726 of the mixed layer by high frequency wind forcing (Eden et al. 2014).

727 The combined TKE + IDEMIX approach was already applied in a couple of publications (Eden et al. 2014,
728 Nielsen et al. 2018, Gutjahr et al. 2020). It was shown in Pollmann et al. 2017 that TKE dissipation rates
729 from the combined TKE+IDEMIX approach are comparable to dissipation rates estimated from Argo floats.
730 In FESOM2.0, the usage of TKE+IDEMIX leads to a significant increase in the tropical and extratropical,
731 and to a decrease in the high-latitude, temperature and salinity over depth when compared to the case of only
732 using `cvmix_TKE`. These differences compensate for some of the biases in the surface and intermediate
733 depth ranges when IDEMIX is not used. The usage of IDEMIX leads to an enhanced heterogeneous
734 representation of vertical mixing especially below the mixed layer along the continental shelves and
735 topographic slopes. However the temperature gain for the deeper depth ranges below 1000 m seems to be
736 strongly overestimated when using `cvmix_TKE+IDEMIX`, hinting at a too strong vertical mixing in the deep
737 ocean. When it comes to the MLD, `cvmix_TKE+IDEMIX` leads in the northern hemisphere to a significant
738 increase in the MLD along the Labrador Sea boundary currents and in the southern GIN seas, which can be
739 attributed to the enhanced mixing along the continental slope of the North Atlantic and in the vicinity of the
740 overflow regions. In the southern hemisphere using IDEMIX leads to an enhancement of the vertical
741 diffusivity along the continental slope of the Weddell Sea. This leads to an enhanced mixing of cold and
742 salty waters, which further reduces the stratification and significantly increases the MLD of the Weddell Sea
743 and to a rather overestimation of the otherwise already high MLD values.

744 This is in contrast to the findings of Gutjahr et al. 2020, who found that in their coupled MPI-ESM1.2
745 simulation, IDEMIX led to a reduction of the vertical mixing in the Weddell Sea allowing for more local
746 stratification. One possibility to overcome the lack of performance of IDEMIX but also of `cvmix_TIDAL` in
747 the Southern Ocean and Weddell Sea could be its combination with partial bottom cells, which had the
748 tendency to significantly reduce the deep convection in the Weddell Sea. At this point it needs further studies

749 also with FESOM2.0 to analyse the different behaviour of IDEMIX that could be influenced by local
750 resolution, coupled ocean-atmosphere feedback or just different background water mass structure.
751 Nevertheless, the achievable energetic consistency with the combined `cvmix_TKE+IDEMIX` approach is an
752 interesting feature that should find more applications in the ocean modelling community, although there is
753 still some way to go to better understand and improve its integration.

754 The last part in this paper deals with the vertical mixing parameterisation MOMIX of Timmermann and
755 Beckmann, (2004) in FESOM2.0 that helped us to overcome some major biases in the model. Since the very
756 beginning of FESOM2.0 the model suffered from a severe cooling and salinification bias in the Southern
757 Ocean and marginal seas around Antarctica, that was accompanied by a strongly overestimated MLD values
758 and too weak stratification in the Weddell Sea. It is shown here that applying MOMIX south of -50°S helped
759 to significantly reduce the biases and bring the MLD depth values in the Weddell Sea into a reasonable
760 range. MOMIX increases the vertical diffusivity within the depth range of the Monin-Obukhov mixing
761 length. This helps the warmer and fresher surface water masses from the melting season to connect with
762 colder and saltier subsurface water masses from the freezing season and thus increase the stratification and
763 reduce the vertical convection. Further, the using of MOMIX in combination with `fesom_KPP` leads to a
764 cooling and freshening in the branch of the NAC that seemed to be connected to a weakening of the upper
765 AMOC cell by 1 Sv and thus to a slight reduction of the meridional heat transport. The reason why
766 FESOM2.0 in the Southern Ocean is so dependent on MOMIX, which was not the case with FESOM1.4,
767 needs further research. Our actual best practise FESOM2.0 configuration uses the `zstar` approach with partial
768 cells and MOMIX switched on as a default, together with `fesom_KPP` for the vertical mixing, although
769 `cvmix_TKE + IDEMIX` shows some promising improvements especially for Arctic applications.

770 To summarize, this paper is the second part of the documentation of the development of important key
771 components of FESOM2.0 in a realistic global model configuration. We described the implementation of
772 partial cells and embedded sea ice and their impact on the modelled hydrography. Furthermore, we briefly
773 described the already existing vertical mixing parameterisation of `fesom_KPP` and `fesom_PP` as well as the
774 newly introduced mixing parameterization of `cvmix_PP`, `cmix_KPP`, `cmix_TIDAL`, `cvmix_TKE` and
775 `cvmix_TKE+IDEMIX` that came with the incorporation of the vertical mixing library CVMix into
776 FESOM2.0.

777 **5 Code availability**

778 The FESOM2.0 version used to carry out the simulations reported here is available on zenodo through
779 <https://doi.org/10.5281/zenodo.4742242>. The used mesh, as well as the temperature, salinity and vertical
780 velocity (for the calculation of the MOC) data of all conducted simulations, can be found under
781 https://swiftbrowser.dkrz.de/tcl_s/hituvPNH3xwiIy/FESOM2.0_evaluation_part2_scholz_etal. Simulated
782 results can of course also be obtained from the authors upon request. Mesh partitioning in FESOM2.0 is
783 based on a METIS version 5.1.0 package developed at the Department of Computer Science and Engineering

45

784 at the University of Minnesota (<http://glaros.dtc.umn.edu/gkhome/views/metis>, last access: 18 November
785 2019). METIS and the pARMS solver (Li et al., 2003) present separate libraries which are freely available
786 subject to their licenses. The Polar Science Center hydrographic climatology (Steele et al., 2001) used for
787 model initialization and the CORE-II atmospheric forcing data (Large and Yeager, 2009) is freely available
788 online. The vertical mixing library CVMix is freely available from <https://github.com/CVMix/CVMix-src> or
789 <https://doi.org/10.5281/zenodo.1000801>

790

791 **Author contributions**

792 SD, DS, PS and NK worked on the development of the FESOM2.0 model code and the tuning of the model.
793 All simulations shown in this paper were carried out by PS who were also responsible for preparing the basic
794 manuscript. QW, SD, NK, DS and TJ have contributed to the final version of the manuscript.

795 **Acknowledgements**

796 This paper is a contribution to the project S2: Improved parameterisations and numerics in climate models,
797 S1: Diagnosis and Metrics in Climate Models and M5: Reducing spurious diapycnal mixing in ocean models
798 of the Collaborative Research Centre TRR 181 “Energy Transfer in Atmosphere and Ocean” funded by the
799 Deutsche Forschungsgemeinschaft (DFG, German Research Foundation) – project no. 274762653, and the
800 Helmholtz initiative REKLIM (Regional Climate Change). This study has benefited from funding from the
801 Initiative and Networking Fund of the Helmholtz Association through the project “Advanced Earth System
802 Modelling Capacity (ESM)”. Dmitry Sein was also supported in the framework of the state assignment of the
803 Ministry of Science and Higher Education of Russia (№0128-2021-0014).

804 **References**

805

- 806 Adcroft, A. and Campin, J.-M.: Rescaled height coordinates for accurate representation of free-surface flows in ocean
807 circulation models, *Ocean Model.*, 7(3–4), 269–284, doi:10.1016/j.ocemod.2003.09.003, 2004.
- 808 Adcroft, A., Hill, C. and Marshall, A. J.: Representation of topography by shaved cells in a height coordinate ocean
809 model, *Mon. Weather Rev.*, 125(9), 2293–2315, doi:10.1175/1520-0493(1997)125<2293:ROTBSC>2.0.CO;2, 1997.
- 810 Barnier, B., Madec, G., Penduff, T., Molines, J.-M., Treguier, A., Le Sommer, J., Beckmann, A., Biastoch, A., Böning,
811 C., Dengg, J., Derval, C., Durand, E., Gulev, S., Remy, E., Talandier, C., Theetten, S., Maltrud, M., McClean, J. and De
812 Cuevas, B.: Impact of partial steps and momentum advection schemes in a global ocean circulation model at eddy-
813 permitting resolution, *Ocean Dyn.*, 56(5–6), 543–567, doi:10.1007/s10236-006-0082-1, 2006.
- 814 Campin, J. M., Marshall, J. and Ferreira, D.: Sea ice-ocean coupling using a rescaled vertical coordinate z^* , *Ocean*
815 *Model.*, 24(1–2), 1–14, doi:10.1016/j.ocemod.2008.05.005, 2008.
- 816 Cavalieri, D. J., Parkinson, C. L., Gloersen, P. and Zwally, H. J.: ea Ice Concentrations from Nimbus-7 SMMR and

46

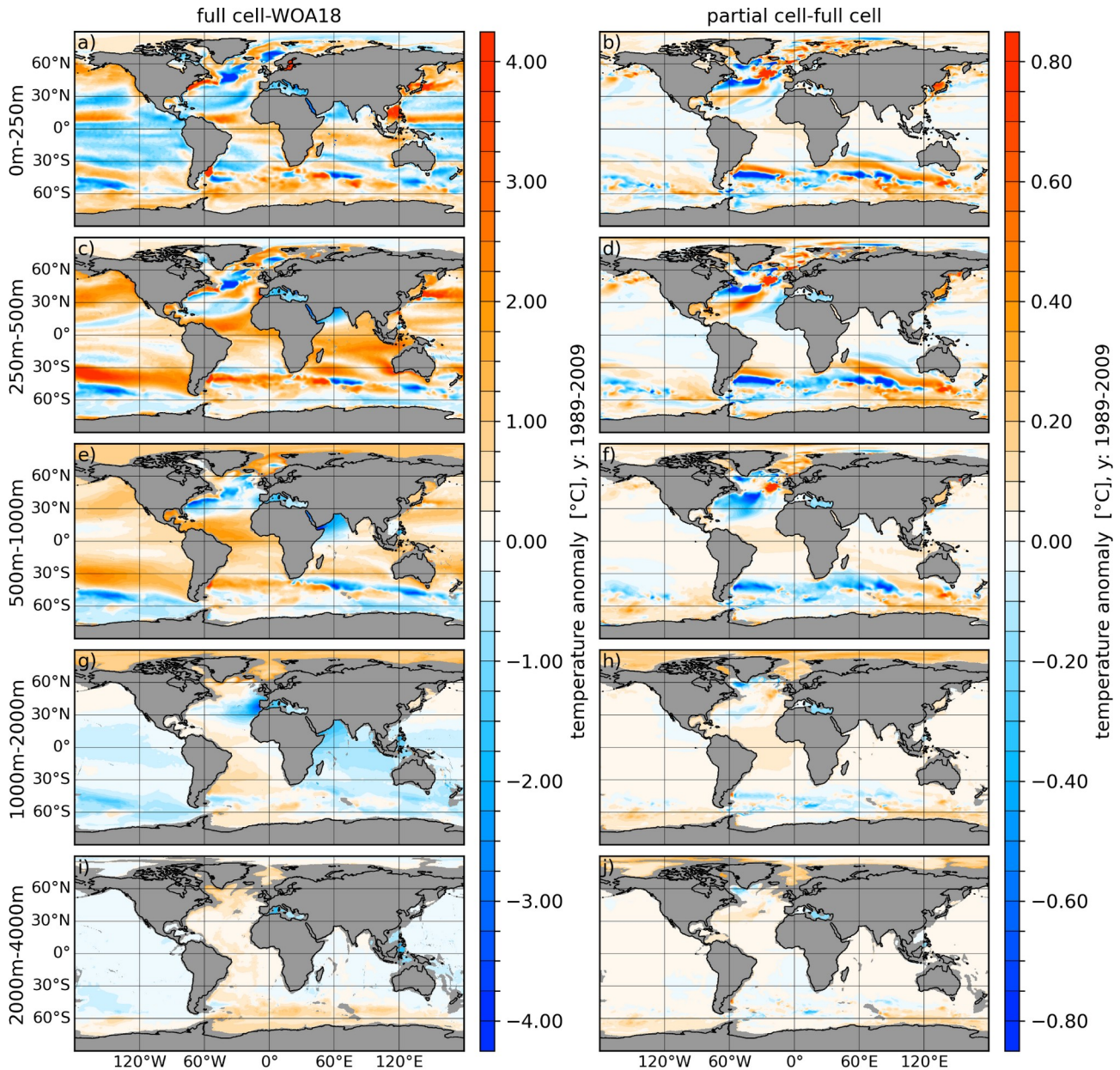
- 817 DMSP SSM/I-SSMIS Passive Microwave Data, Version 1. [Indicate subset used], doi:10.5067/8GQ8LZQVL0VL,
818 1996.
- 819 Cox, M. D.: A numerical ocean model with improved bottom topographic representation, GFDL/NOAA Tech. Rep., 27
820 pp. [Available from Princet. Univ. Princeton, New Jersey 08540.], 1977.
- 821 Danabasoglu, G., Yeager, S. G., Bailey, D., Behrens, E., Bentsen, M., Bi, D., Biastoch, A., Böning, C., Bozec, A.,
822 Canuto, V. M., Cassou, C., Chassignet, E., Coward, A. C., Danilov, S., Diansky, N., Drange, H., Farneti, R., Fernandez,
823 E., Fogli, P. G., Forget, G., Fujii, Y., Griffies, S. M., Gusev, A., Heimbach, P., Howard, A., Jung, T., Kelley, M., Large,
824 W. G., Leboissetier, A., Lu, J., Madec, G., Marsland, S. J., Masina, S., Navarra, A., George Nurser, A. J., Pirani, A., y
825 Mélia, D. S., Samuels, B. L., Scheinert, M., Sidorenko, D., Treguier, A. M., Tsujino, H., Uotila, P., Valcke, S.,
826 Voltaire, A. and Wang, Q.: North Atlantic simulations in Coordinated Ocean-ice Reference Experiments phase II
827 (CORE-II). Part I: Mean states, *Ocean Model.*, 73, 76–107, doi:10.1016/j.ocemod.2013.10.005, 2014.
- 828 Danilov, S., Sidorenko, D., Wang, Q. and Jung, T.: The Finite-volume Sea ice–Ocean Model (FESOM2), *Geosci.*
829 *Model Dev.*, 10(2), 765–789, doi:10.5194/gmd-10-765-2017, 2017.
- 830 Eden, C. and Olbers, D.: An energy compartment model for propagation, nonlinear interaction, and dissipation of
831 internal gravity waves, *J. Phys. Oceanogr.*, 44(8), 2093–2106, doi:10.1175/JPO-D-13-0224.1, 2014.
- 832 Eden, C., Czeschel, L. and Olbers, D.: Toward Energetically Consistent Ocean Models, *J. Phys. Oceanogr.*, 44, 3160–
833 3184, doi:10.1175/JPO-D-13-0260.1, 2014.
- 834 Ferrari, R., Griffies, S. M., Nurser, A. J. G. and Vallis, G. K.: A boundary-value problem for the parameterized
835 mesoscale eddy transport, *Ocean Model.*, 32(3–4), 143–156, doi:10.1016/j.ocemod.2010.01.004, 2010.
- 836 Fox-kemper, B., Adcroft, A., Böning, C. W., Chassignet, E. P., Gerdes, R., Greatbatch, R. J., Griffies, S. M. and
837 Hallberg, R. W.: Challenges and Prospects in Ocean Circulation Models, , 6(February), 1–29,
838 doi:10.3389/fmars.2019.00065, 2019.
- 839 Fox-Kemper, B. and Menemenlis, D.: Can large eddy simulation techniques improve mesoscale rich ocean models?, in
840 *Ocean Modeling in an Eddying Regime*, Volume 177, edited by M. W. Hecht and H. Hasumi, pp. 319–337., 2008.
- 841 Gaspar, P., Goris, Y. G. R. I. and Lefevre, J.: A Simple Eddy Kinetic Energy Model for Simulations of the Oceanic
842 Vertical Mixing ' Tests at Station Papa and Long-Term Upper Ocean Study Site, , 95, 179–193, 1990.
- 843 Gent, P. R. and McWilliams, J. C.: Isopycnal Mixing in Ocean Circulation Models, *J. Phys. Oceanogr.*, 20(1), 150–155,
844 doi:10.1175/1520-0485(1990)020<0150:IMIOCM>2.0.CO;2, 1990.
- 845 Gent, P. R., Willebrand, J., McDougall, T. J. and McWilliams, J. C.: Parameterizing Eddy-Induced Tracer Transports in
846 Ocean Circulation Models, *J. Phys. Oceanogr.*, 25(4), 463–474, doi:10.1175/1520-
847 0485(1995)025<0463:PEITTI>2.0.CO;2, 1995.
- 848 Griffies, S. M., Böning, C., Bryan, F. O., Chassignet, E. P., Gerdes, R., Hasumi, H., Hirst, A., Treguier, A. M. and
849 Webb, D.: Developments in ocean climate modelling, *Ocean Model.*, 2(3–4), 123–192, doi:10.1016/s1463-
850 5003(00)00014-7, 2000.
- 851 Griffies, S. M., Levy, M., Adcroft, A. J., Danabasoglu, G., Hallberg, R. W., Jacobsen, D., Large, W. and Ringler, T.:
852 Theory and numerics of the Community Ocean Vertical Mixing (CVMix) project., 2015.
- 853 Gutjahr, O., Putrasahan, D., Lohmann, K., Jungclaus, J. H., Von Storch, J. S., Brüggemann, N., Haak, H. and Stössel,
854 A.: Max Planck Institute Earth System Model (MPI-ESM1.2) for the High-Resolution Model Intercomparison Project
855 (HighResMIP), *Geosci. Model Dev.*, 12(7), 3241–3281, doi:10.5194/gmd-12-3241-2019, 2019.
- 856 Gutjahr, O., Brüggemann, N., Haak, H., Jungclaus, J. H., Putrasahan, D. A., Lohmann, K. and von Storch, J.-S.:
857 Comparison of ocean vertical mixing schemes in the Max Planck Institute Earth System Model (MPI-ESM1.2), *Geosci.*
858 *Model Dev.*, in review, doi:https://doi.org/10.5194/gmd-2020-202, 2020.

- 859 Hibler, W., Heil, P. and Lytle, V. I.: On simulating high frequency variability in Antarctic sea-ice dynamics models,
860 *Ann. Glaciol.*, 27, 443-448, 1998.
- 861 Hutchings, J. K., Heil, P. and Hibler, W. D.: Modeling Linear Kinematic Features in Sea Ice, *Mon. Wea. Rev.* , 3481-
862 3497, <https://doi.org/10.1175/MWR3045.1>, 2005.
- 863 Ilicak, M., Drange, H., Wang, Q., Gerdes, R., Aksenov, Y., Bailey, D., Bentsen, M., Biastoch, A., Bozec, A., Böning,
864 C., Cassou, C., Chassignet, E., Coward, A. C., Curry, B., Danabasoglu, G., Danilov, S., Fernandez, E., Fogli, P. G.,
865 Fujii, Y., Griffies, S. M., Iovino, D., Jahn, A., Jung, T., Large, W. G., Lee, C., Lique, C., Lu, J., Masina, S., George
866 Nurser, A. J., Roth, C., Salas y Mélia, D., Samuels, B. L., Spence, P., Tsujino, H., Valcke, S., Voldoire, A., Wang, X.
867 and Yeager, S. G.: An assessment of the Arctic Ocean in a suite of interannual CORE-II simulations. Part III:
868 Hydrography and fluxes, *Ocean Model.*, 100, 141–161, doi:10.1016/j.ocemod.2016.02.004, 2016.
- 869 Jayne, S. R. and St. Laurent, L. C.: Tidal Dissipation over Rough, *Geophys. Res. Lett.*, 28(5), 811–814, 2001.
- 870 Käse, R. H., Biastoch, A. and Stammer, D. B.: On the mid-depth circulation in the Labrador and Irminger Seas,
871 *Geophys. Res. Lett.*, 28(18), 3433–3436, doi:10.1029/2001GL013192, 2001.
- 872 Koldunov, N. V., Danilov, S., Sidorenko, D., Hutter, N., Losch, M., Goessling, H., et al., Fast EVP solutions in a high-
873 resolution sea ice model. *Journal of Advances in Modeling Earth Systems*, 11, 1269– 1284.
874 doi.org/10.1029/2018MS00148, 2019
- 875 Large, W. G. and Yeager, S. G.: The global climatology of an interannually varying air - Sea flux data set, *Clim. Dyn.*,
876 33(2–3), 341–364, doi:10.1007/s00382-008-0441-3, 2009.
- 877 Large, W. G., McWilliams, J. C. and Doney, S. C.: Oceanic vertical mixing: A review and a model with a nonlocal
878 boundary layer parameterization, *Rev. Geophys.*, 32(4), 363, doi:10.1029/94RG01872, 1994.
- 879 Lemke, P.: A coupled one-dimensional sea ice-ocean model, , 92(C12), 164–172,
880 doi:<https://doi.org/10.1029/JC092iC12p13164>, 1987.
- 881 Locarnini, R. A., Mishonov, A. V., Baranova, O. K., Boyer, T. P., Zweng, M. M., Garcia, H. E., Reagan, J. R., Seidov,
882 D., Weathers, K., Paver, C. R. and Smolyar, I.: World Ocean Atlas 2018, Volume 1: Temperature, A. Mishonov Tech.
883 Ed.; NOAA Atlas NESDIS 81, 52, 2018.
- 884 Maier-Reimer, E., Mikolajewicz, U. and Hasselmann, K.: Mean circulation of the Hamburg LSG OGCM and its
885 sensitivity to the thermohaline surface forcing, *J. Phys. Oceanogr.*, 23(4), 731–757, doi:10.1175/1520-
886 0485(1993)023<0731:MCOTHL>2.0.CO;2, 1993.
- 887 Marshall, J. and Schott, F.: Open-ocean convection: Observations, theory, and models, *Rev. Geophys.*, 37(1), 1–64,
888 doi:10.1029/98RG02739, 1999.
- 889 Myers, P. G.: SPOM: A regional model of the sub-polar north Atlantic, *Atmos. - Ocean*, 40(4), 445–463,
890 doi:10.3137/ao.400405, 2002.
- 891 Nielsen, S. B., Jochum, M., Eden, C. and Nuterman, R.: An energetically consistent vertical mixing parameterization in
892 CCSM4, *Ocean Model.*, 127, 46–54, doi:10.1016/j.ocemod.2018.03.002, 2018.
- 893 Nielsen, S. B., Jochum, M., Pedro, J. B., Eden, C. and Nuterman, R.: Two-Timescale Carbon Cycle Response to an
894 AMOC Collapse, *Paleoceanogr. Paleoclimatology*, 34(4), 511–523, doi:10.1029/2018PA003481, 2019.
- 895 Olbers, D. and Eden, C.: A Global Model for the Diapycnal Diffusivity Induced by Internal Gravity Waves, , 1759–
896 1779, doi:10.1175/JPO-D-12-0207.1, 2013.
- 897 Pacanowski, R. C. and Gnanadesikan, A.: Transient response in a Z-level ocean model that resolves topography with
898 partial cells, *Mon. Weather Rev.*, 126(12), 3248–3270, doi:10.1175/1520-0493(1998)126<3248:TRIAZL>2.0.CO;2,
899 1998.

- 900 Pacanowski, R. C. and Philander, S. G. H.: Parameterization of Vertical Mixing in Numerical Models of Tropical
 901 Oceans, *J. Phys. Oceanogr.*, 11(11), 1443–1451, doi:10.1175/1520-0485(1981)011<1443:POVMIN>2.0.CO;2, 1981.
- 902 Pollmann, F., Eden, C. and Olbers, D.: Evaluating the Global internal wave model IDEMIX using finestructure
 903 methods, *J. Phys. Oceanogr.*, 47(9), 2267–2289, doi:10.1175/JPO-D-16-0204.1, 2017.
- 904 Redi, M. H.: Oceanic Isopycnal Mixing by Coordinate Rotation, *J. Phys. Oceanogr.*, 12(10), 1154–1158,
 905 doi:10.1175/1520-0485(1982)012<1154:OIMBCR>2.0.CO;2, 1982.
- 906 Robertson, R. and Dong, C.: An evaluation of the performance of vertical mixing parameterizations for tidal mixing in
 907 the Regional Ocean Modeling System (ROMS), *Geosci. Lett.*, 6(1), 1–18, doi:10.1186/s40562-019-0146-y, 2019.
- 908 Rousset, C., Vancoppenolle, M., Madec, G., Fichefet, T., Flavoni, S., Barthélemy, A., Benshila, R., Chanut, J., Levy,
 909 C., Masson, S. and Vivier, F.: The Louvain-La-Neuve sea ice model LIM3.6: Global and regional capabilities, *Geosci.
 910 Model Dev.*, 8(10), 2991–3005, doi:10.5194/gmd-8-2991-2015, 2015.
- 911 Sallée, J. B., Shuckburgh, E., Bruneau, N., Meijers, A. J. S., Bracegirdle, T. J. and Wang, Z.: Assessment of Southern
 912 Ocean mixed-layer depths in CMIP5 models: Historical bias and forcing response, *J. Geophys. Res. Ocean.*, 118(4),
 913 1845–1862, doi:10.1002/jgrc.20157, 2013.
- 914 Scholz, P., Sidorenko, D., Gurses, O., Danilov, S., Koldunov, N., Wang, Q., Sein, D., Smolentseva, M., Rakowsky, N.
 915 and Jung, T.: Assessment of the Finite-volumE Sea ice-Ocean Model (FESOM2.0) -- Part 1: Description of selected key
 916 model elements and comparison to its predecessor version, *Geosci. Model Dev.*, 12(11), 4875–4899, doi:10.5194/gmd-
 917 12-4875-2019, 2019.
- 918 Semmler, T., Danilov, S., Gierz, P., Goessling, H. F., Hegewald, J., Hinrichs, C., Koldunov, N., Khosravi, N., Mu, L.,
 919 Rackow, T., Sein, D. V., Sidorenko, D., Wang, Q. and Jung, T.: Simulations for CMIP6 With the AWI Climate Model
 920 AWI-CM-1-1, *J. Adv. Model. Earth Syst.*, 12(9), 1–34, doi:10.1029/2019MS002009, 2020.
- 921 Semtner, A. J. and Mintz, Y.: Numerical simulation of the Gulf Stream and mid-ocean eddies., *J. Phys. Oceanogr.*, 7(2,
 922 Mar. 1977), 208–230, doi:10.1175/1520-0485(1977)007<0208:nsotgs>2.0.co;2, 1977.
- 923 Shchepetkin, A. F.: A method for computing horizontal pressure-gradient force in an oceanic model with a nonaligned
 924 vertical coordinate, *J. Geophys. Res.*, 108(C3), 3090, doi:10.1029/2001JC001047, 2003.
- 925 Simmons, H. L., Jayne, S. R., St, L. C. and Weaver, A. J.: Tidally driven mixing in a numerical model of the ocean
 926 general circulation, , 6, 245–263, doi:10.1016/S1463-5003(03)00011-8, 2004.
- 927 Steele, M., Morley, R. and Ermold, W.: PHC: A global ocean hydrography with a high-quality Arctic Ocean, *J. Clim.*,
 928 14(9), 2079–2087, doi:10.1175/1520-0442(2001)014<2079:PAGOHW>2.0.CO;2, 2001.
- 929 Timmermann, R. and Beckmann, A.: Parameterization of vertical mixing in the Weddell Sea, *Ocean Model.*, 6(1), 83–
 930 100, doi:10.1016/S1463-5003(02)00061-6, 2004.
- 931 Van Roekel, L., Adcroft, A. J., Danabasoglu, G., Griffies, S. M., Kauffman, B., Large, W., Levy, M., Reichl, B. G.,
 932 Ringler, T. and Schmidt, M.: The KPP Boundary Layer Scheme for the Ocean: Revisiting Its Formulation and
 933 Benchmarking One-Dimensional Simulations Relative to LES, *J. Adv. Model. Earth Syst.*, 10(11), 2647–2685,
 934 doi:10.1029/2018MS001336, 2018.
- 935 Vernet, M., Geibert, W., Hoppema, M., Brown, P. J., Haas, C. and Hellmer, H. H.: The Weddell Gyre , Southern
 936 Ocean : Present Knowledge and Future Challenges Reviews of Geophysics, *Rev. Geophys.*, 57, 623–708,
 937 doi:10.1029/2018RG000604, 2019.
- 938 Wang, Q., Danilov, S., Sidorenko, D., Timmermann, R., Wekerle, C., Wang, X., Jung, T. and Schröter, J.: The Finite
 939 Element Sea Ice-Ocean Model (FESOM) v.1.4: formulation of an ocean general circulation model, *Geosci. Model Dev.*,
 940 7(2), 663–693, doi:10.5194/gmd-7-663-2014, 2014.
- 941

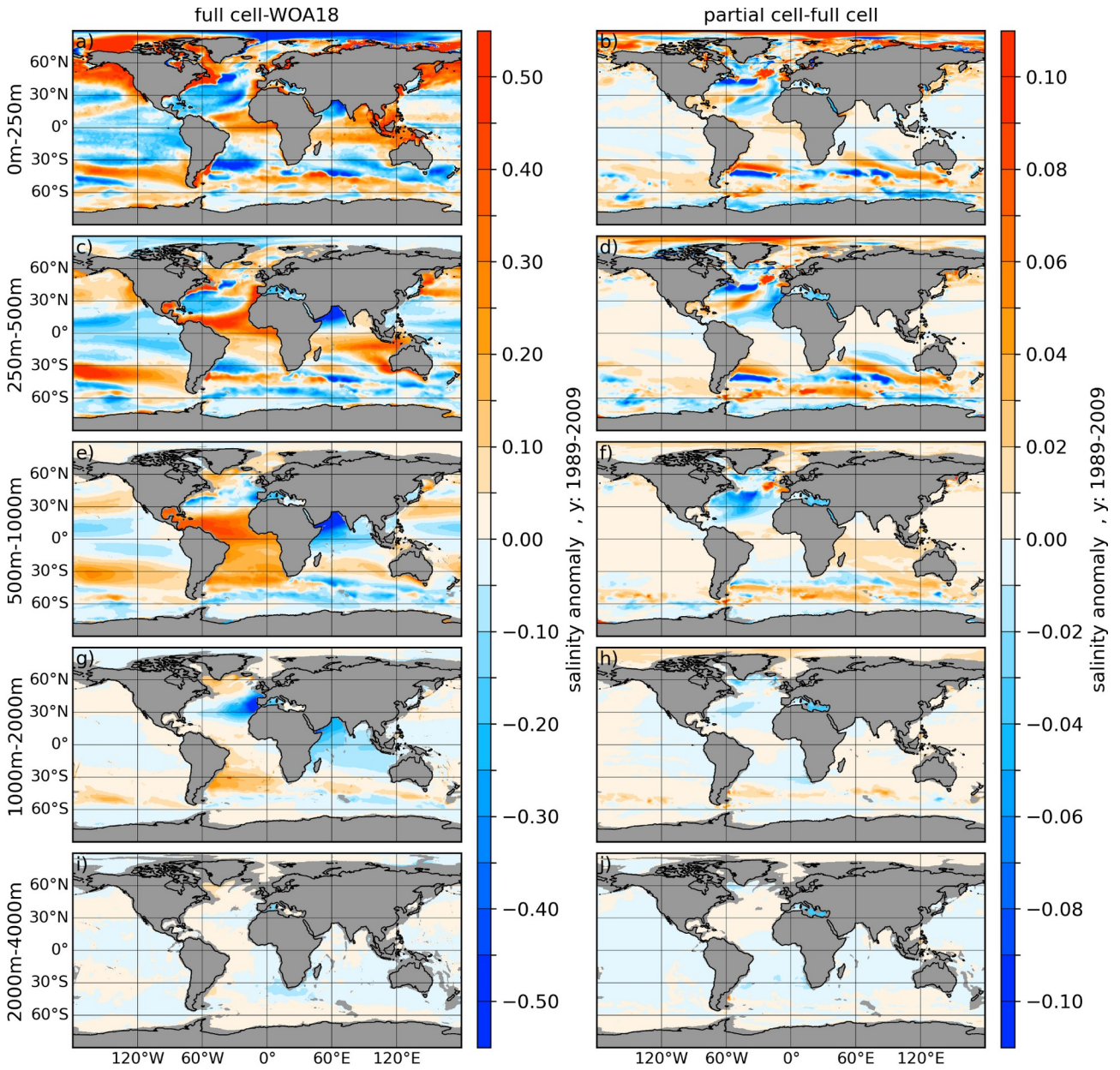
942 Zweng, M. M., Reagan, J. R., Seidov, D., Boyer, T. P., Locarnini, R. A., Garcia, H. E., Mishonov, A. V., Baranova, O.
 943 K., Weathers, K., Paver, C. R. and Smolyar, I.: World Ocean Atlas 2018, Volume 2: Salinity, A. Mishonov Tech. Ed.;
 944 NOAA Atlas NESDIS 82, 50, 2018.

945



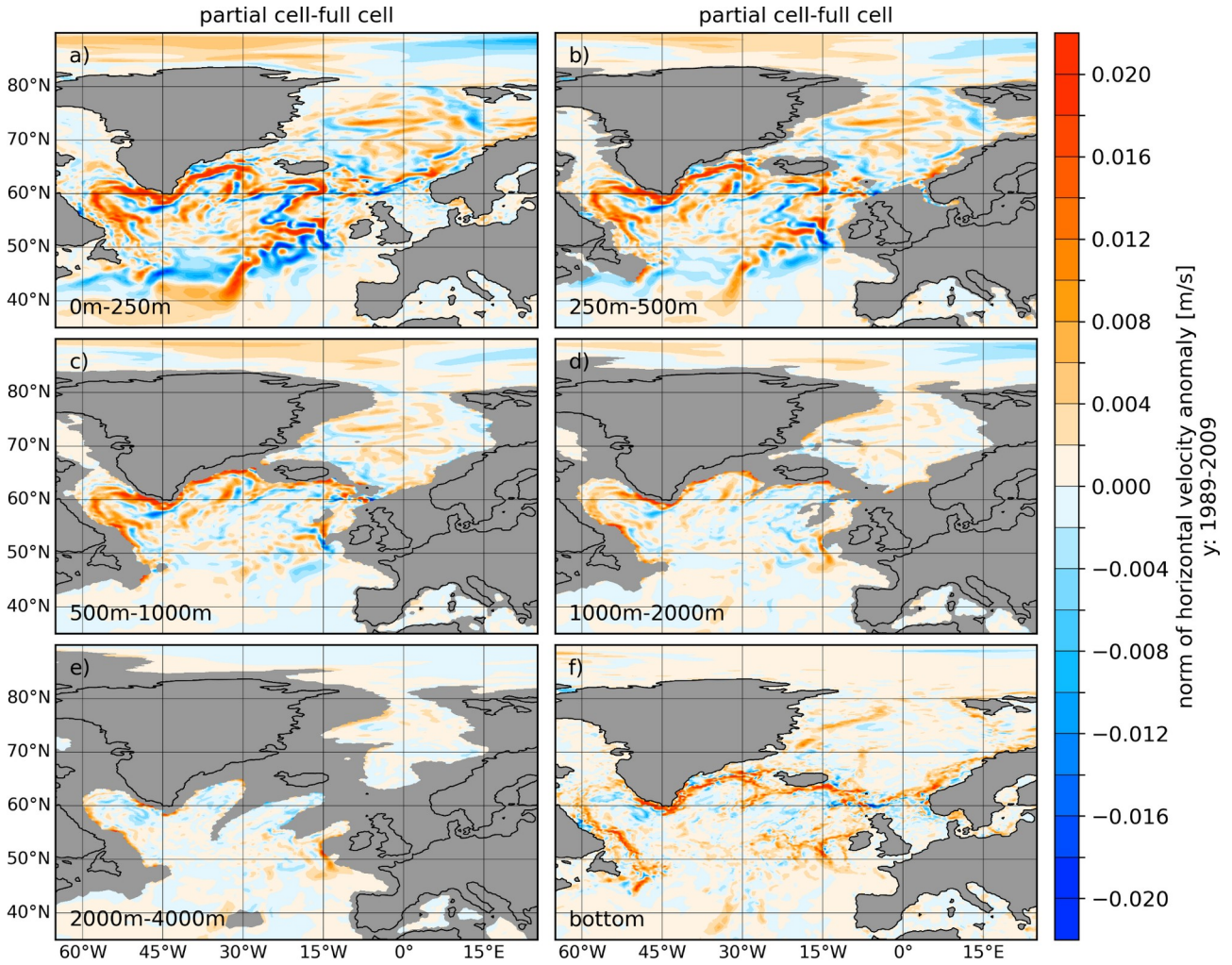
946 **Figure 1:** (Left column) Temperature biases full cells referenced to the World Ocean Atlas 2018 (WOA18,
 947 Zweng et. al 2018) averaged over the period 1989-2009. The right column shows the temperature difference
 948 between partial and full cells (partial minus full). From top to bottom the panels show the vertically averaged
 949 fields for the depth ranges of 0-250 m, 250-500 m, 500-1000 m, 1000-2000 m and 2000-4000 m.
 950
 951

952

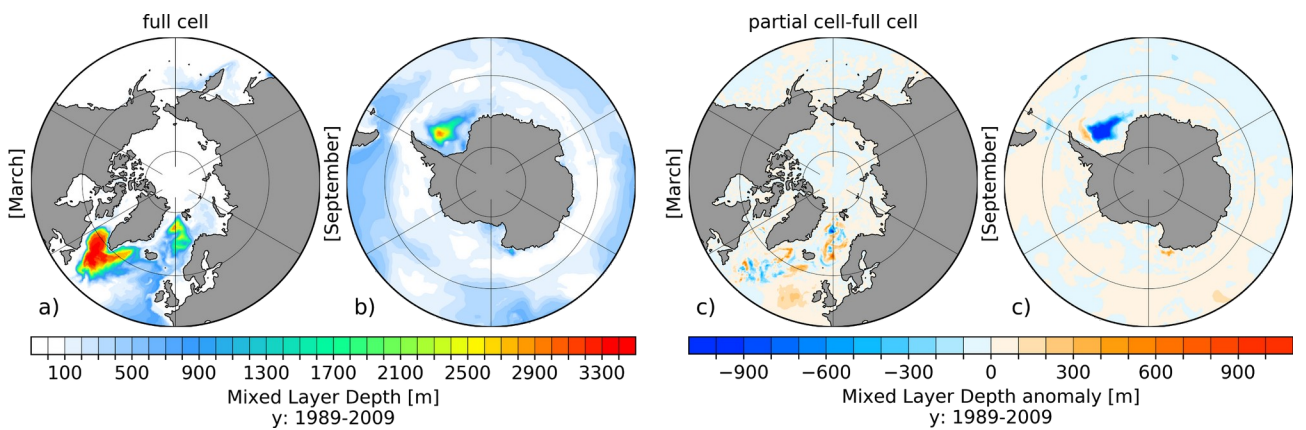


953

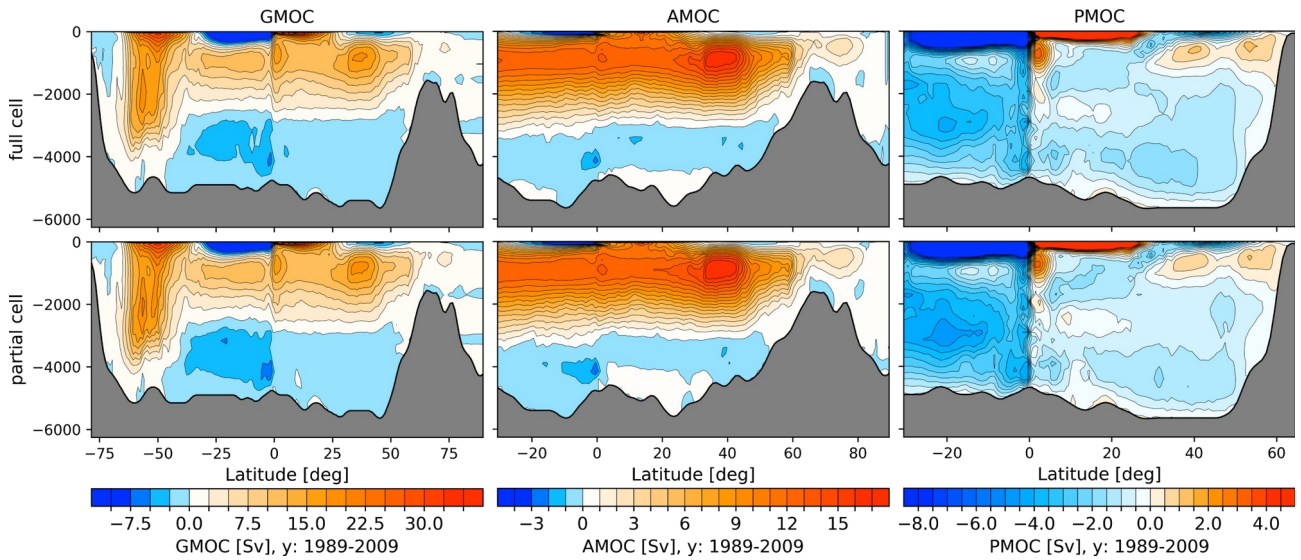
954 **Figure 2:** Same as Fig. 1, but for salinity.



955 **Figure 3:** Difference of the horizontal velocity norm between simulations with partial and full cells (partial-
 956 full) averaged over the period 1989-2009 and averaged over the depth ranges of 0-250 m, 250-500 m, 500-
 957 1000 m, 1000-2000 m and 2000-4000 m as well as the bottom value.
 958
 959
 960



961 **Figure 4:** Northern hemispheric March (a) and southern Hemispheric September (b) mixed layer depth
 962 (MLD) with full cells as well as corresponding anomalous MLD with partial minus full cells (c, d), averaged
 963 for the period 1989-2009.
 964

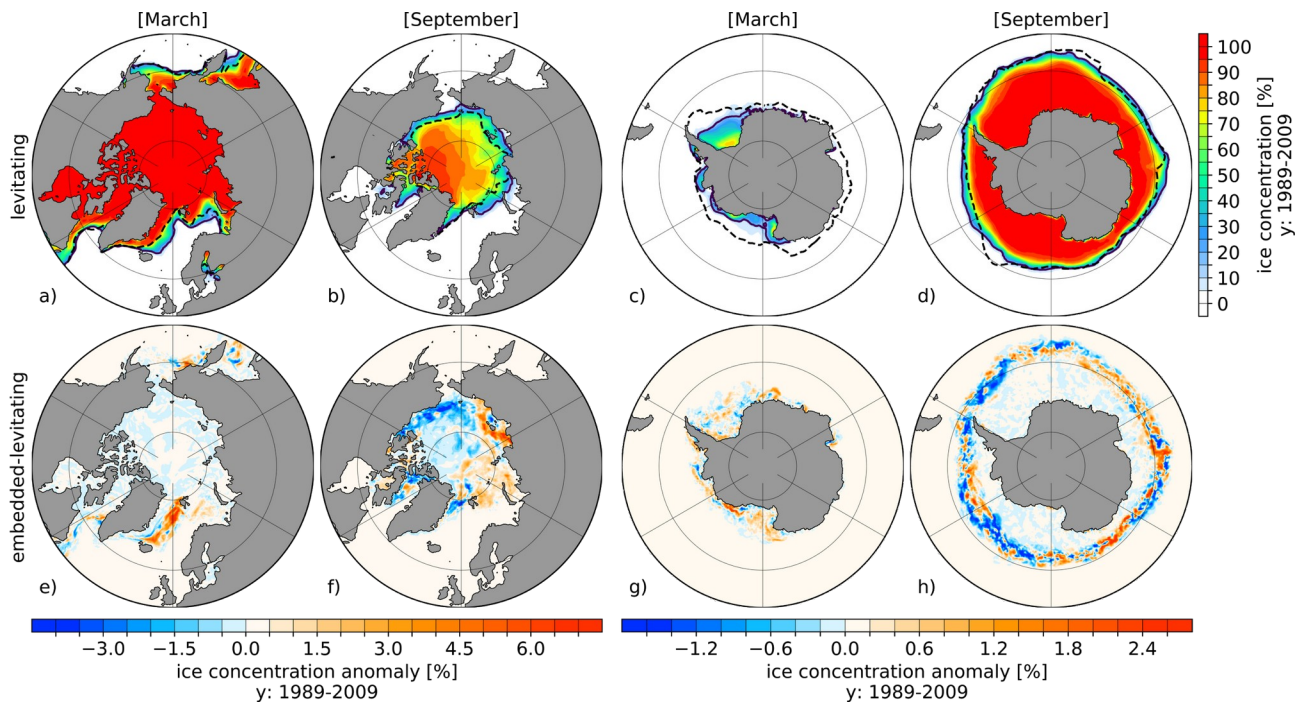


965

966 **Figure 5:** Global (GMOC, left column), Atlantic (AMOC, middle column) and Indo-Pacific (PMOC, right
 967 column) Meridional Overturning Circulation for full cell (upper row) and partial cell (lower row) averaged
 968 for the time period 1989-2009.

969

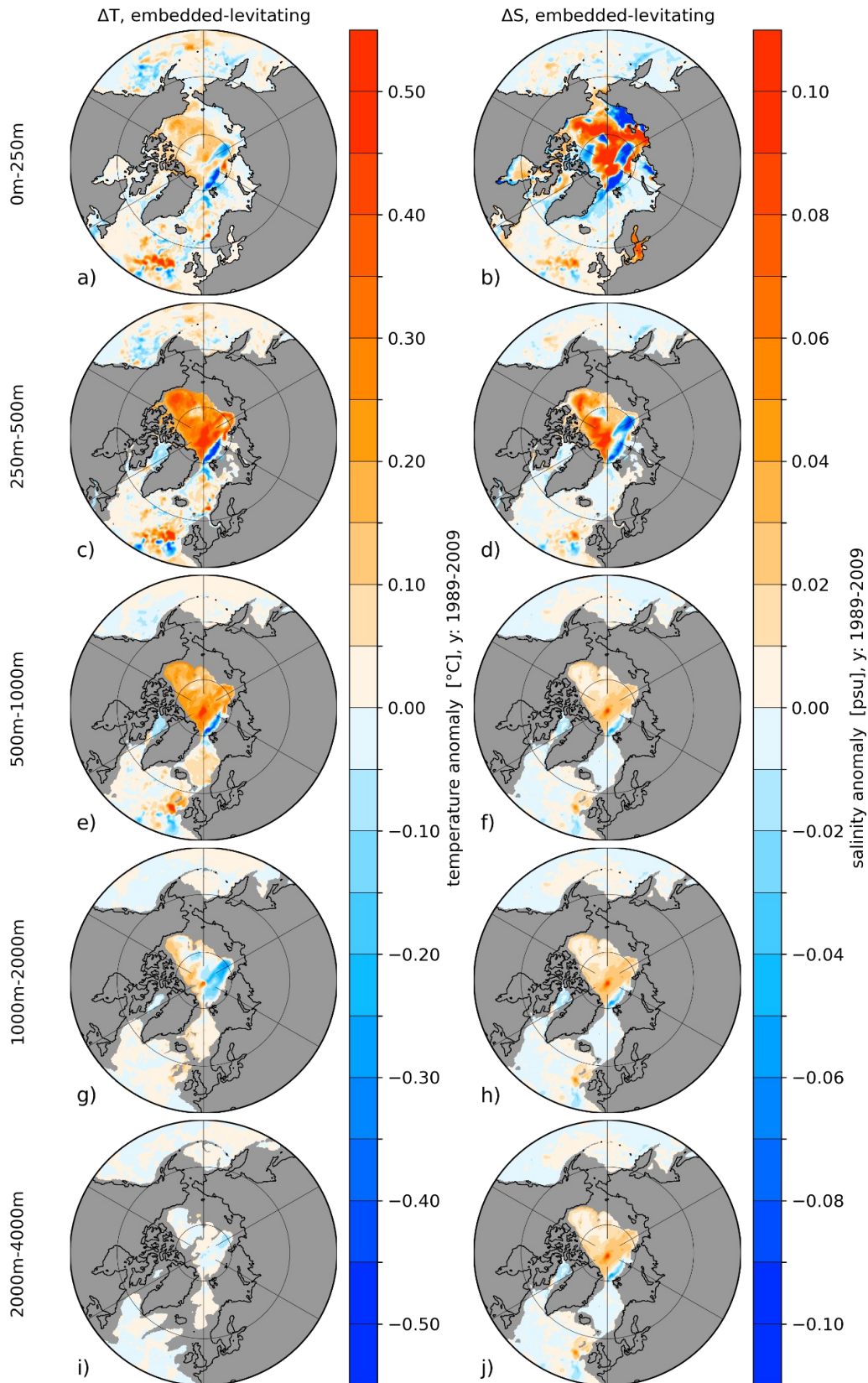
970



971

972 **Figure 6:** Levitating (upper row) northern and southern hemispheric March (a, c) and September (b, d) sea
 973 ice concentration averaged for the period 1989-2009. Solid and dashed lines indicate the simulated and
 974 observed (Cavaliere et al., 1996) contour of the 15% sea ice extent. The lower row shows the corresponding
 975 sea ice concentration anomalies between embedded and levitating sea ice (embedded minus levitating)
 976 averaged over the same period.

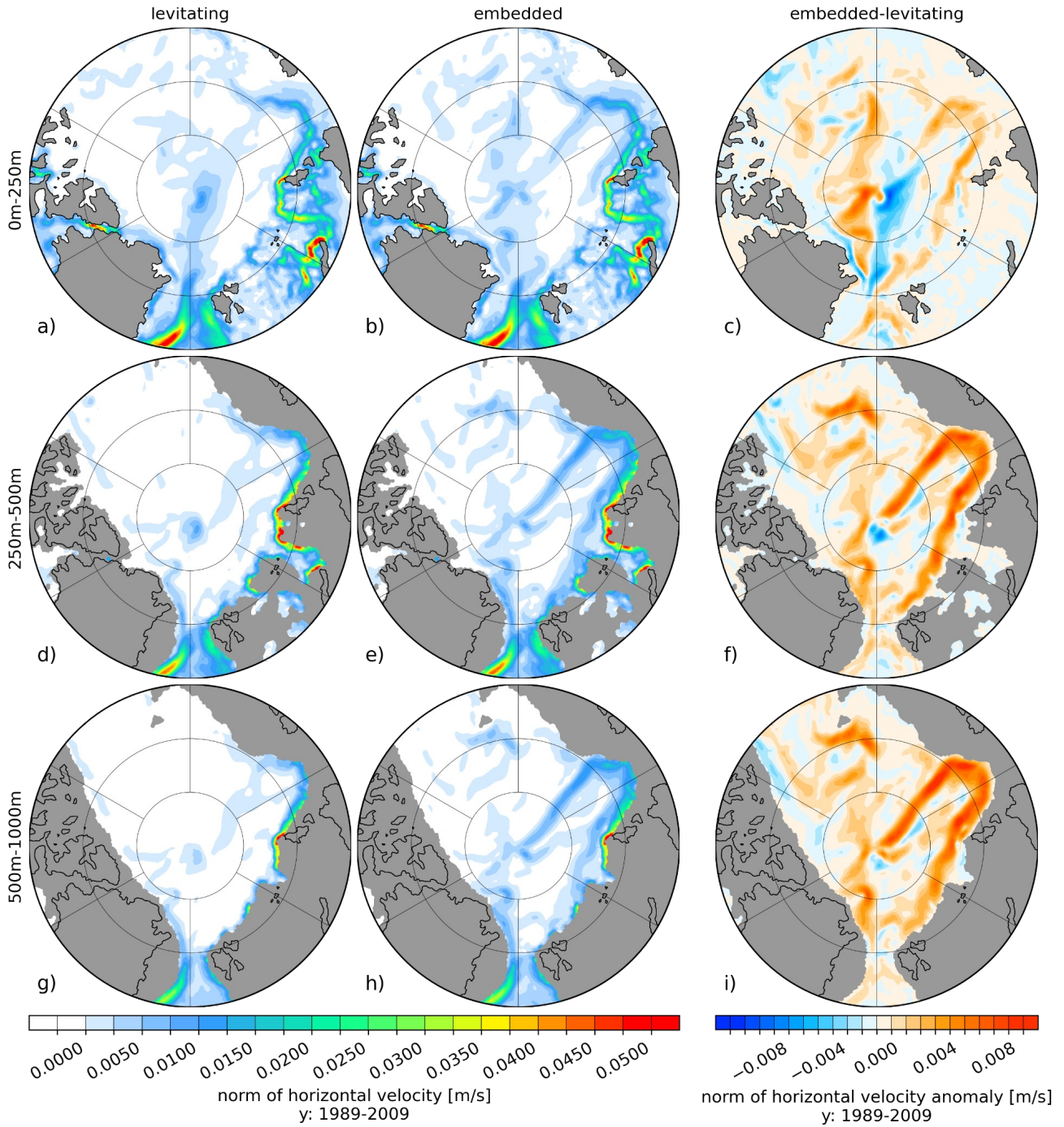
977



978

979 **Figure 7:** Temperature (left column) and salinity (right column) difference between embedded- and
 980 levitating sea ice averaged for the period 1989 to 2009. From top to bottom, panels show the vertically
 981 averaged fields for the depth ranges of 0-250 m, 250-500 m, 500-1000 m, 1000-2000 m and 2000-4000 m.
 982

982



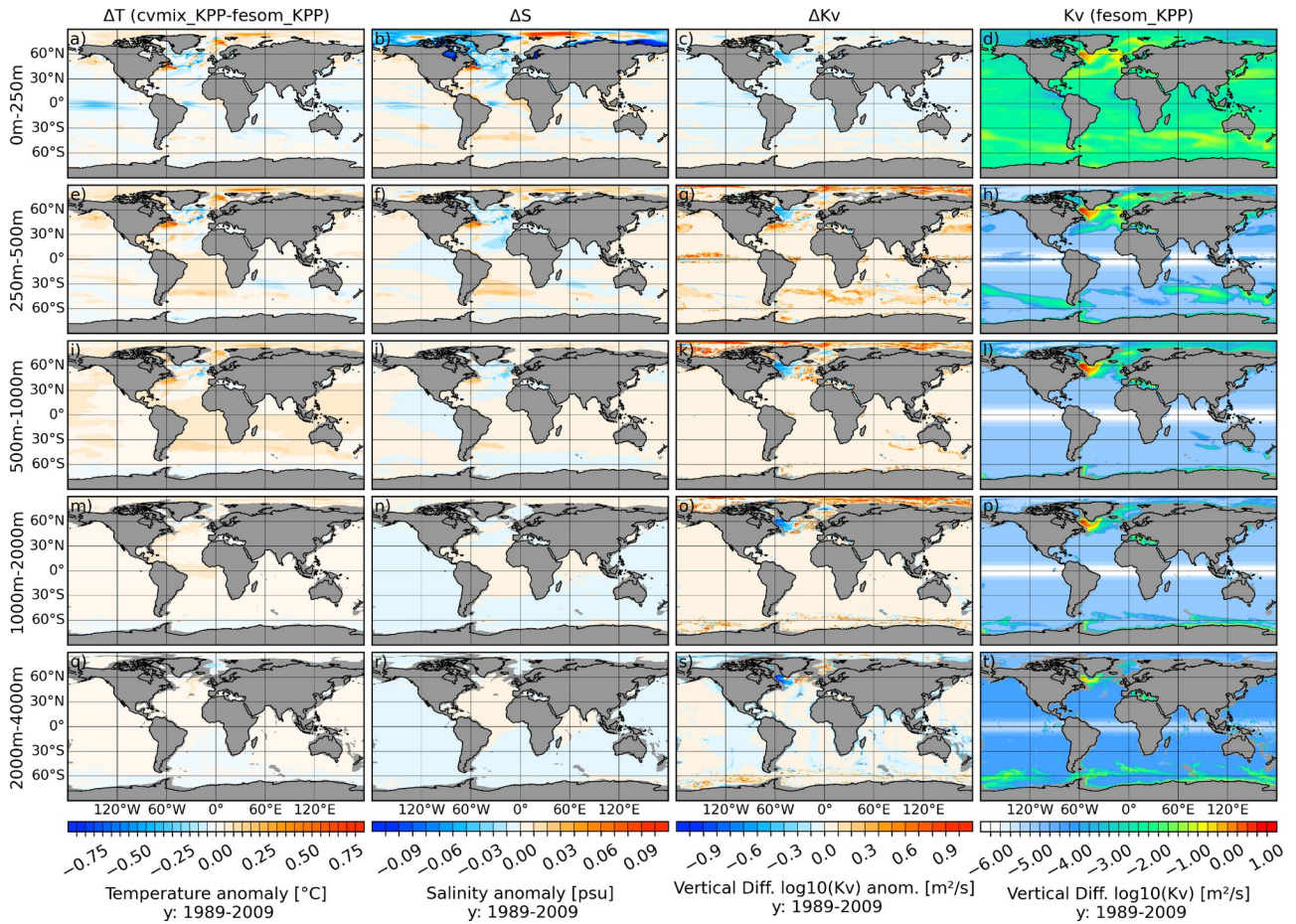
983

984 **Figure 8:** Norm of ocean velocity for levitating (left column) and floating (middle column) and the
 985 difference between embedded and levitating (right column) sea ice averaged for the period 1989 to 2009.
 986 From top to bottom, the panels show the vertically averaged fields for the depth ranges of 0-250 m, 250-500
 987 m and 500-1000 m.

988

989

990

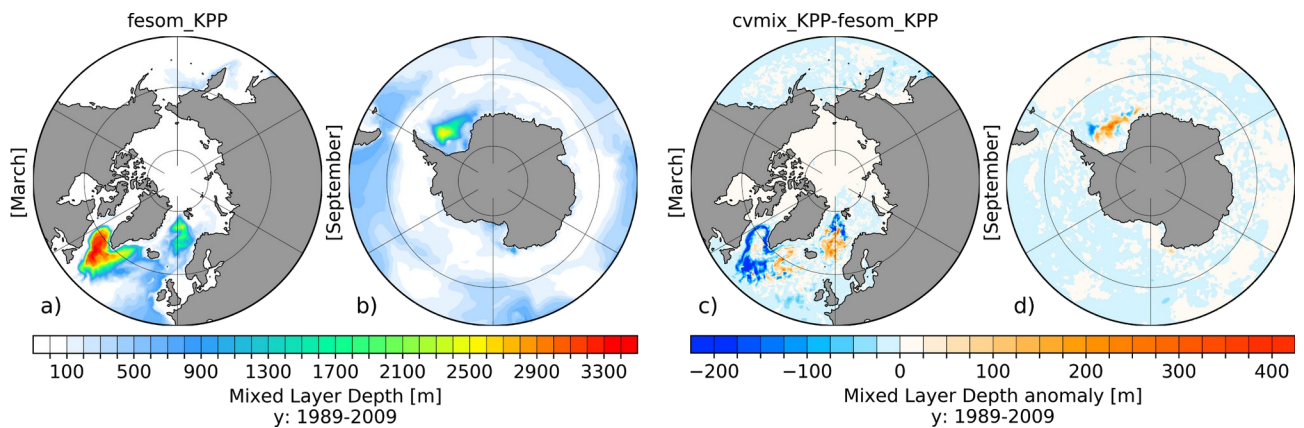


991

992 **Figure 9:** Temperature (1st Column), salinity (2nd column) and vertical diffusivity (3rd column) difference
 993 between cvmix_KPP and original fesom_KPP implementation as well as the absolute vertical diffusivity
 994 values (4th column) for fesom_KPP averaged for the period 1989 to 2009. From top to bottom, panels show
 995 the vertically averaged fields for the depth ranges of 0-250 m, 250-500 m, 500-1000 m, 1000-2000 m and
 996 2000-4000 m.

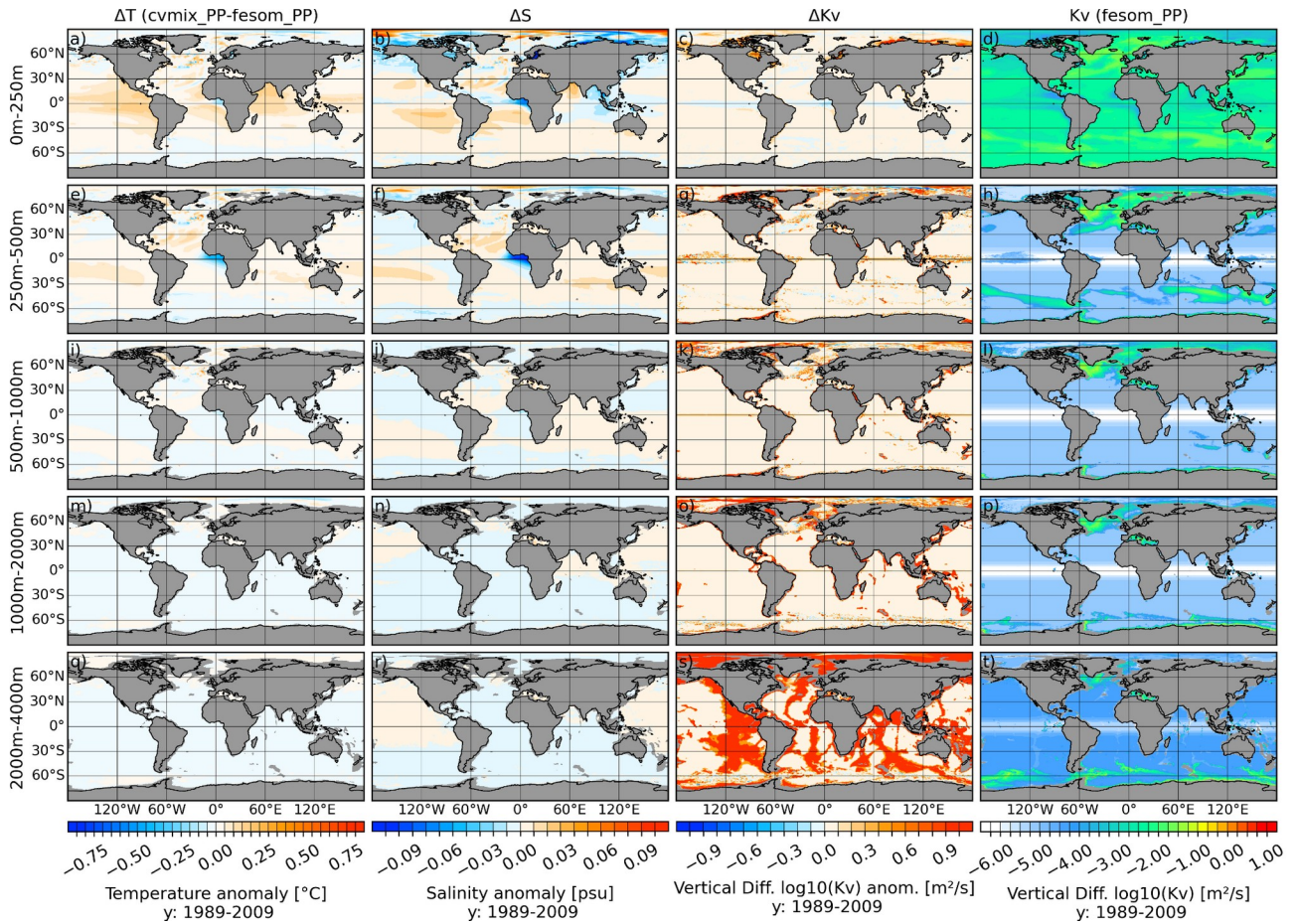
997

998



999

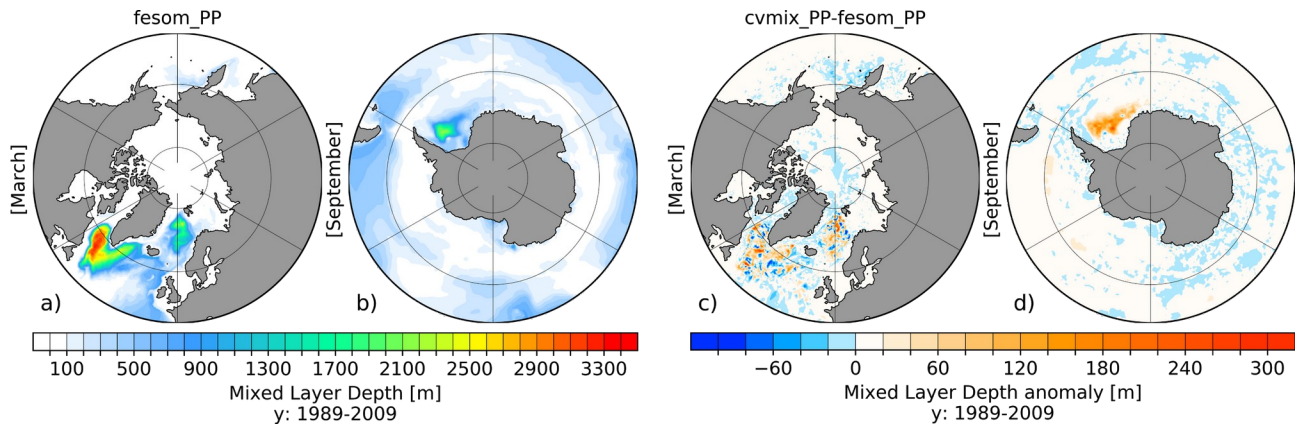
1000 **Figure 10:** Northern hemispheric March (a) and southern Hemispheric September (b) mixed layer depth
 1001 (MLD) for fesom_KPP implementation as well as corresponding anomalous MLD between cvmix_KPP and
 1002 fesom_KPP implementation (c, d), averaged for the period 1989-2009.



1003

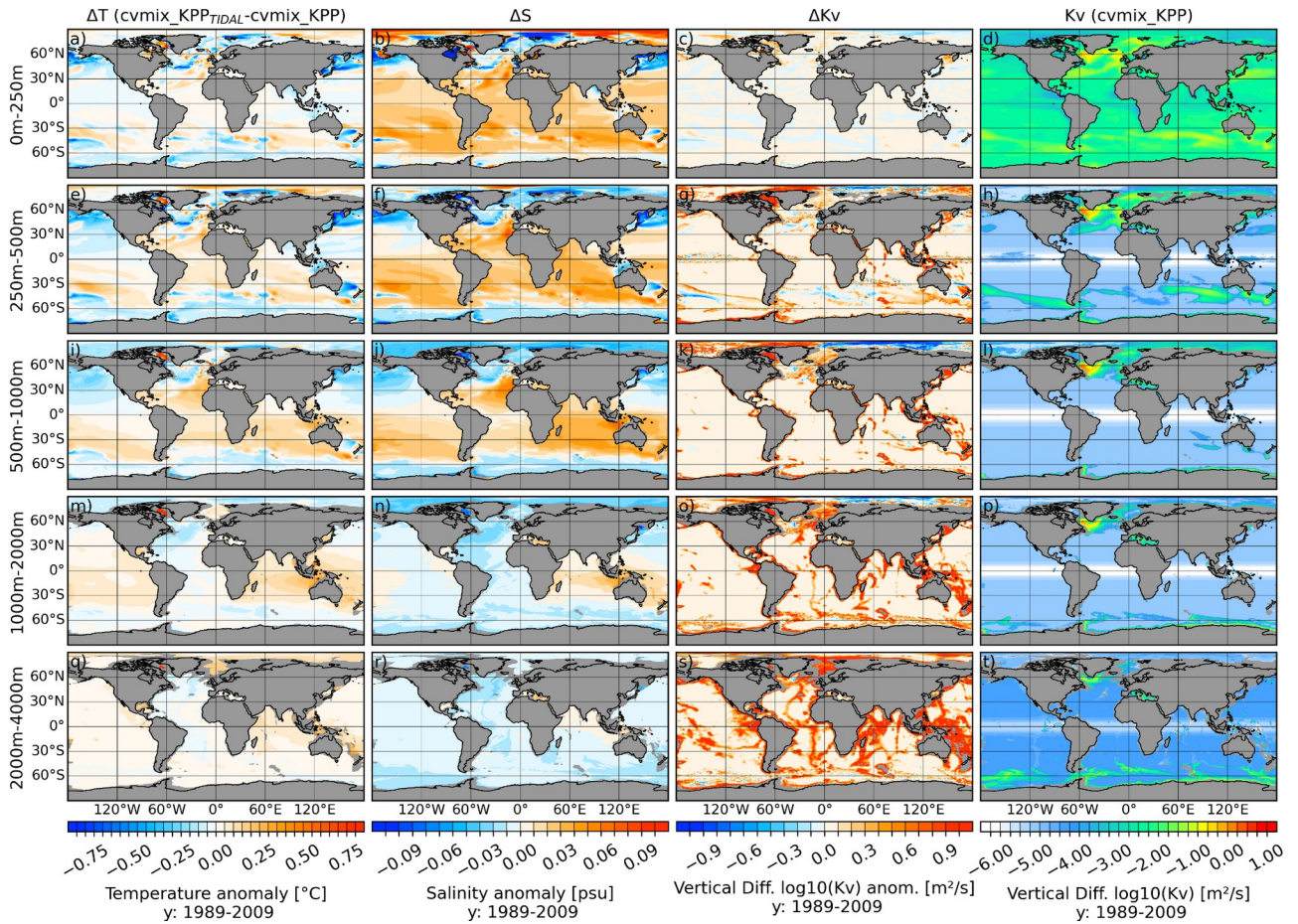
1004 **Figure 11:** Temperature (1st Column), salinity (2nd column) and vertical diffusivity (3rd column) difference
 1005 between `cvmix_PP` and original `fesom_PP` implementation as well as the absolute vertical diffusivity values
 1006 (4th column) for `fesom_PP` averaged for the period 1989 to 2009. From top to bottom, panels show the
 1007 vertically averaged fields for the depth ranges of 0-250 m, 250-500 m, 500-1000 m, 1000-2000 m and 2000-
 1008 4000 m.

1009



1010

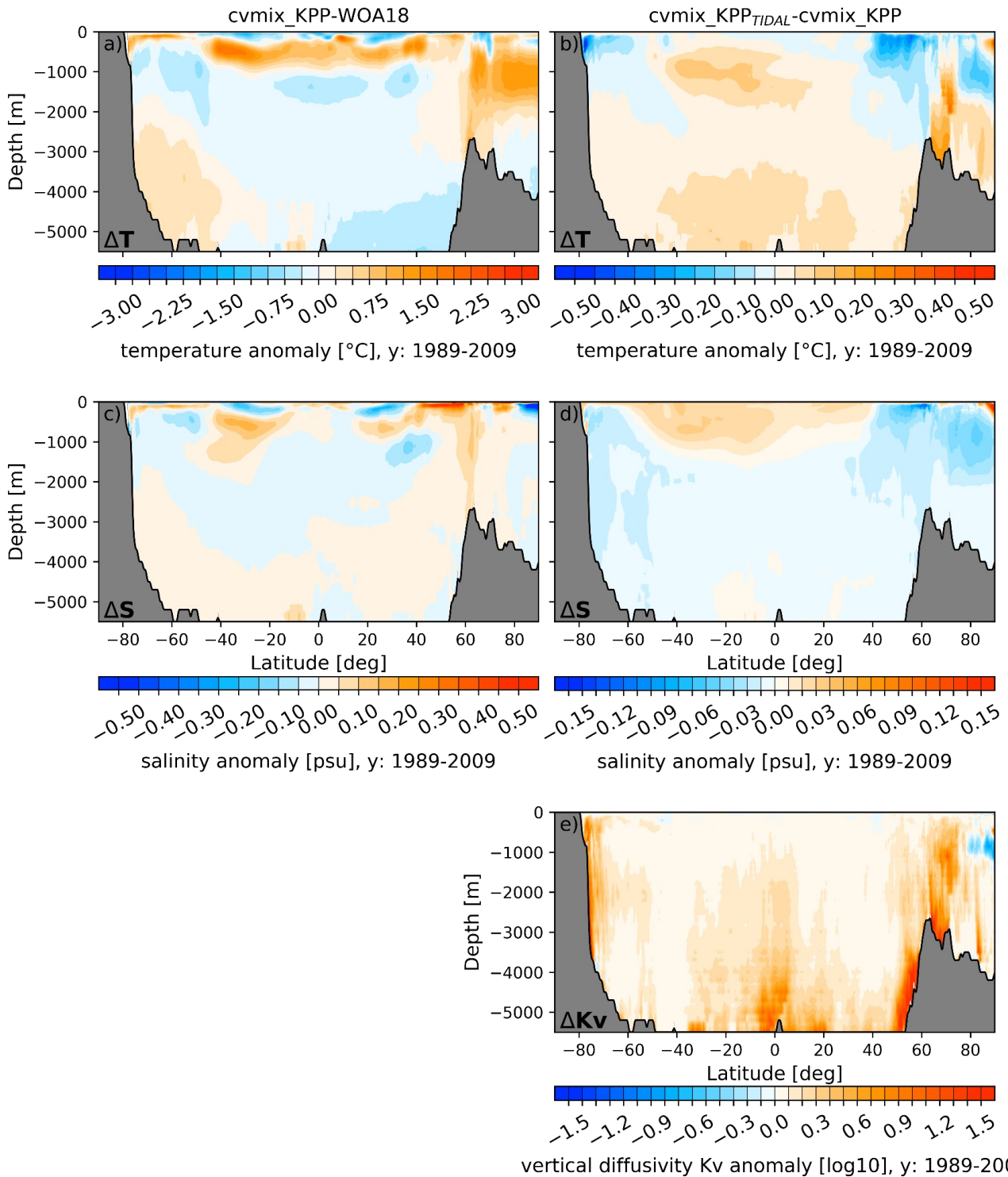
1011 **Figure 12:** Northern hemispheric March (a) and southern Hemispheric September (b) mixed layer depth
 1012 (MLD) for `fesom_PP` implementation as well as corresponding anomalous MLD between `cvmix_PP` and
 1013 `fesom_PP` implementation (c, d), averaged for the period 1989-2009.



1014

1015 **Figure 13:** Temperature (1st Column), salinity (2nd column) and vertical diffusivity (3rd column) difference
 1016 between cvmix_KPP with and without TIDAL mixing of Simmons et al. (2004) as well as the absolute
 1017 vertical diffusivity values (4th column) for cvmix_KPP without TIDAL mixing averaged for the period 1989
 1018 to 2009. From top to bottom, panels show the vertically averaged fields for the depth ranges of 0-250 m,
 1019 250-500 m, 500-1000 m, 1000-2000 m and 2000-4000 m.

1020



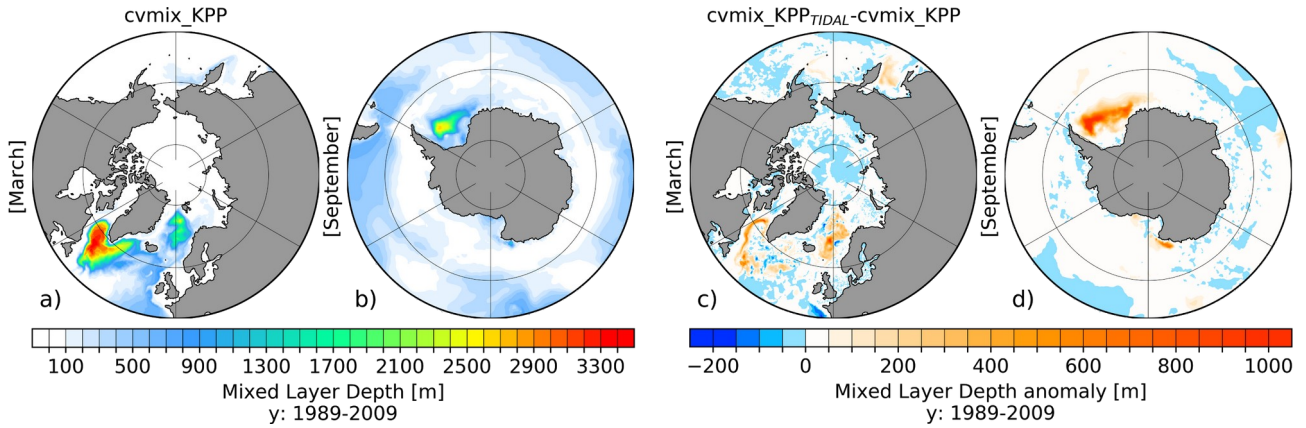
1021

1022 **Figure 14:** Left column: presents global zonal averaged climatological temperature (a) and salinity (c) bias
 1023 profiles of *cvmix_KPP* with respect to WOA18. Right column: shows the global zonal averaged biases of
 1024 temperature (b), salinity (d) and vertical diffusivity (e) between *cvmix_KPP* with tidal mixing of Simmons
 1025 et al. (2004) versus without.

1026

1027

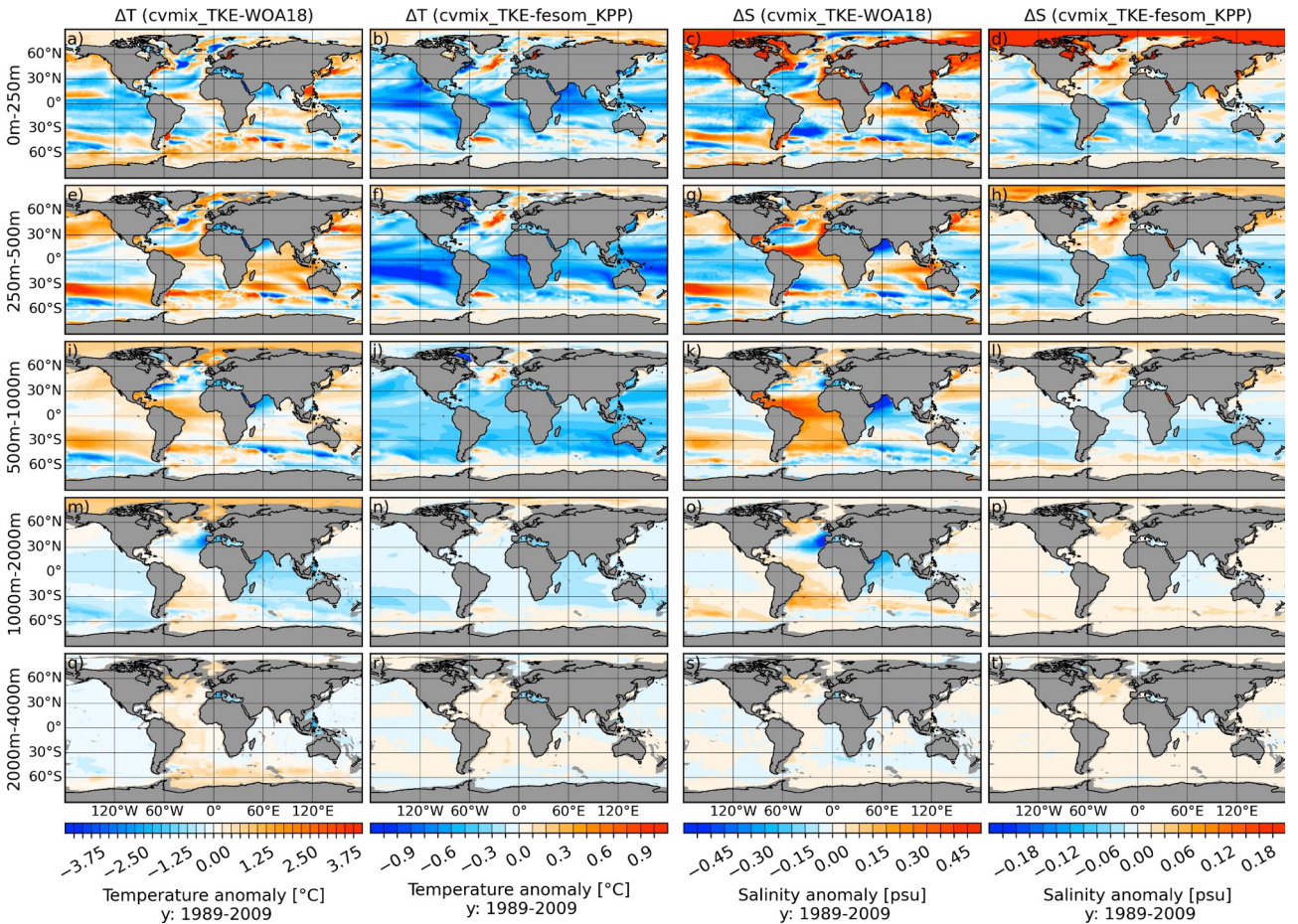
1028



1029

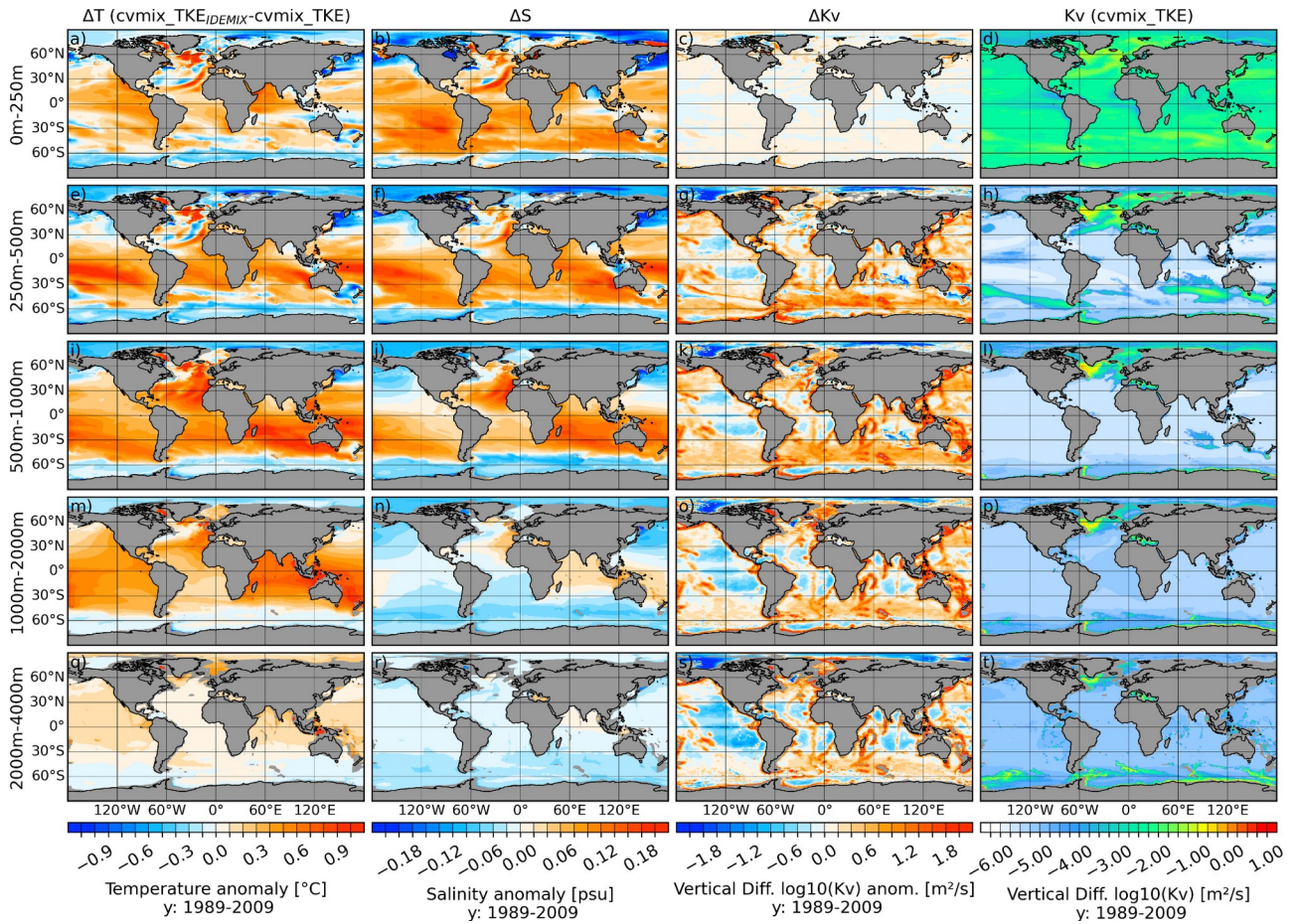
1030 **Figure 15:** Northern hemispheric March (a) and southern Hemispheric September (b) mixed layer depth
 1031 (MLD) for cvmix_KPP without TIDAL mixing as well as corresponding anomalous MLD between
 1032 cvmix_KPP with minus without TIDAL mixing of Simmons et al. (2004)(c, d), averaged for the period
 1033 1989-2009.

1034



1035

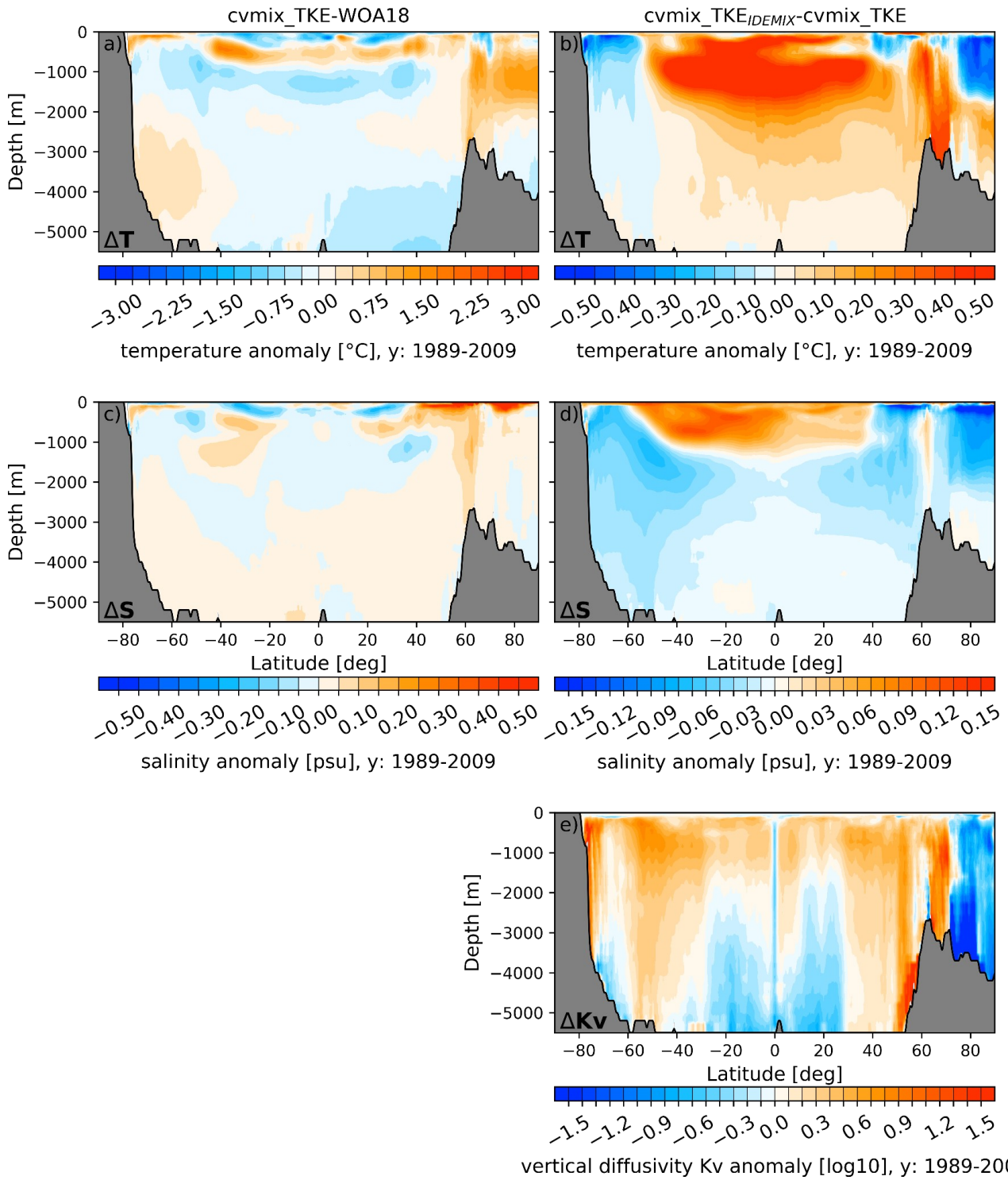
1036 **Figure 16:** Temperature (1st and 2nd column), salinity (3rd and 4th column) difference between cvmix_TKE
 1037 and WOA18 (1st and 3rd column) as well as between cvmix_TKE and fesom_KPP (2nd and 4th column)
 1038 averaged for the period 1989 to 2009. From top to bottom, panels show the vertically averaged fields for the
 1039 depth ranges of 0-250 m, 250-500 m, 500-1000 m, 1000-2000 m and 2000-4000 m.
 1040



1041

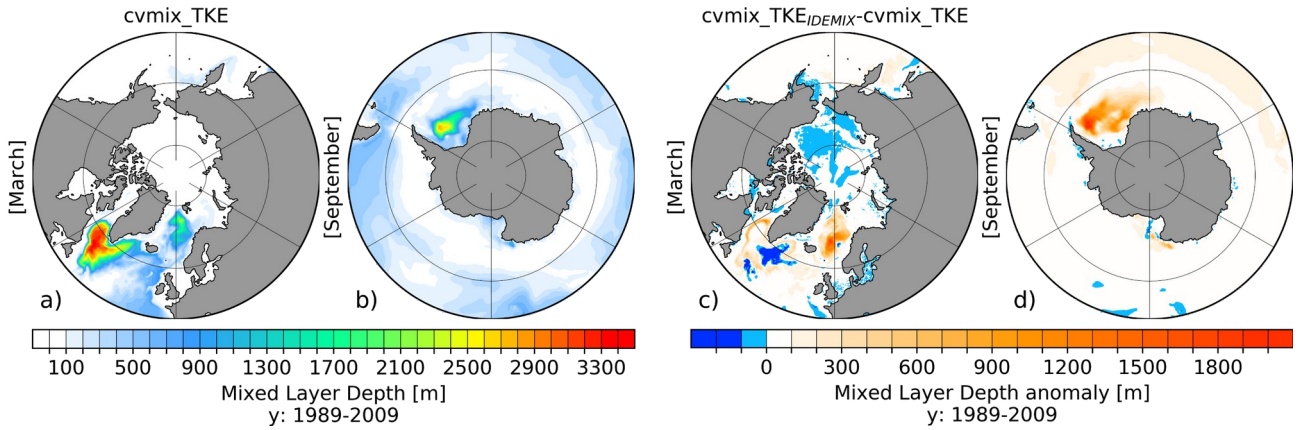
1042 **Figure 17:** Temperature (1st Column), salinity (2nd column) and vertical diffusivity (3rd column) difference
 1043 between cvmix_TKE with and without IDEMIX as well as the absolute vertical diffusivity values (4th
 1044 column) for cvmix_TKE without IDEMIX mixing averaged for the period 1989 to 2009. From top to
 1045 bottom, panels show the vertically averaged fields for the depth ranges of 0-250 m, 250-500 m, 500-1000 m,
 1046 1000-2000 m and 2000-4000 m.

1047



1048

1049 **Figure 18:** Left column: presents global zonal averaged climatological temperature (a) and salinity (c) bias
 1050 profiles of cvmix_TKE with respect to WOA18. Right column: shows the global zonal averaged biases of
 1051 temperature (b), salinity (d) and vertical diffusivity (e) between cvmix_TKE with IDEMIX versus without.

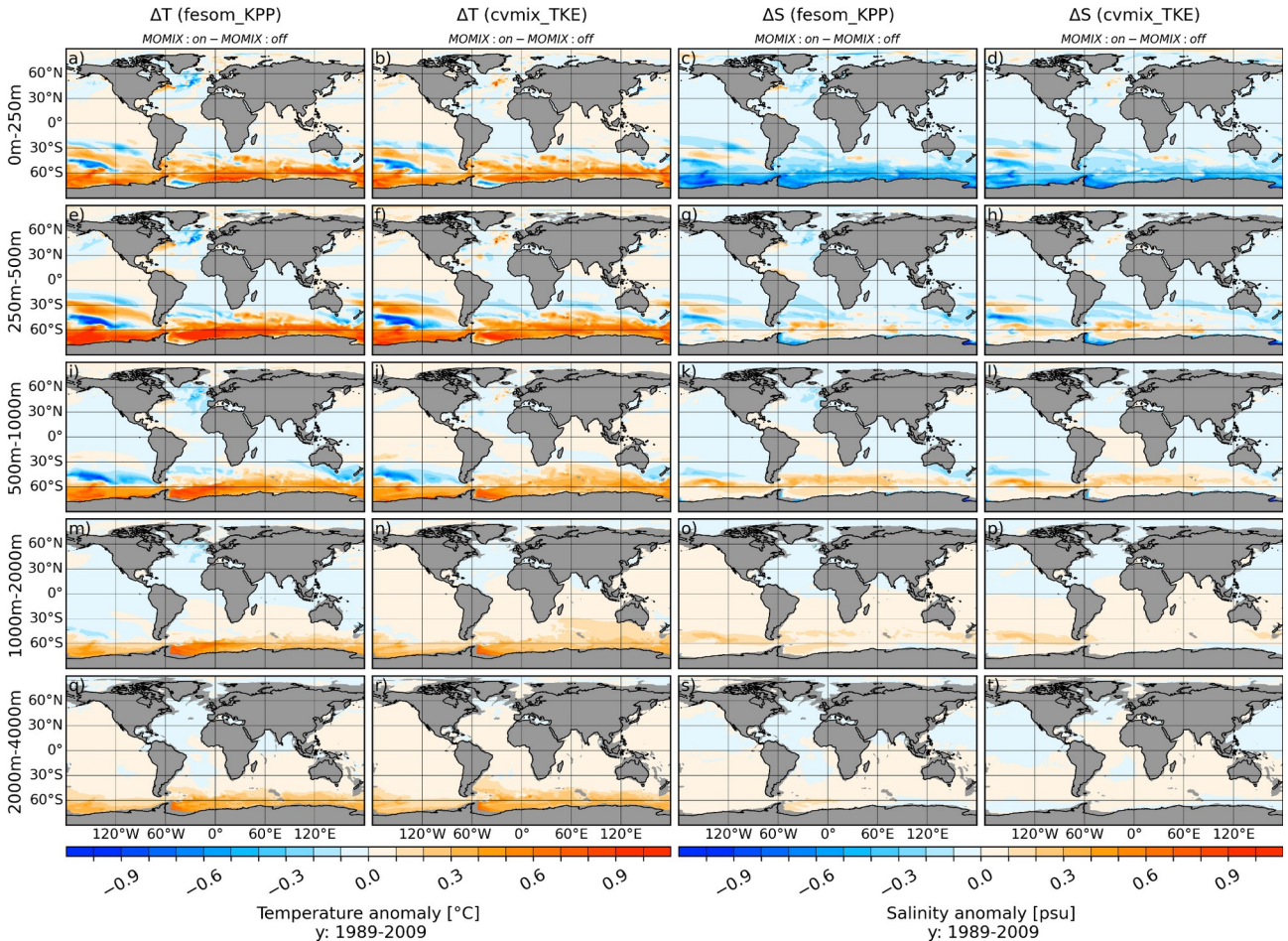


1052

1053 **Figure 19:** Northern hemispheric March (a) and southern Hemispheric September (b) mixed layer depth
 1054 (MLD) for cvmix_TKE without IDEMIX mixing as well as corresponding anomalous MLD between
 1055 cvmix_TKE with minus without IDEMIX mixing, averaged for the period 1989-2009.

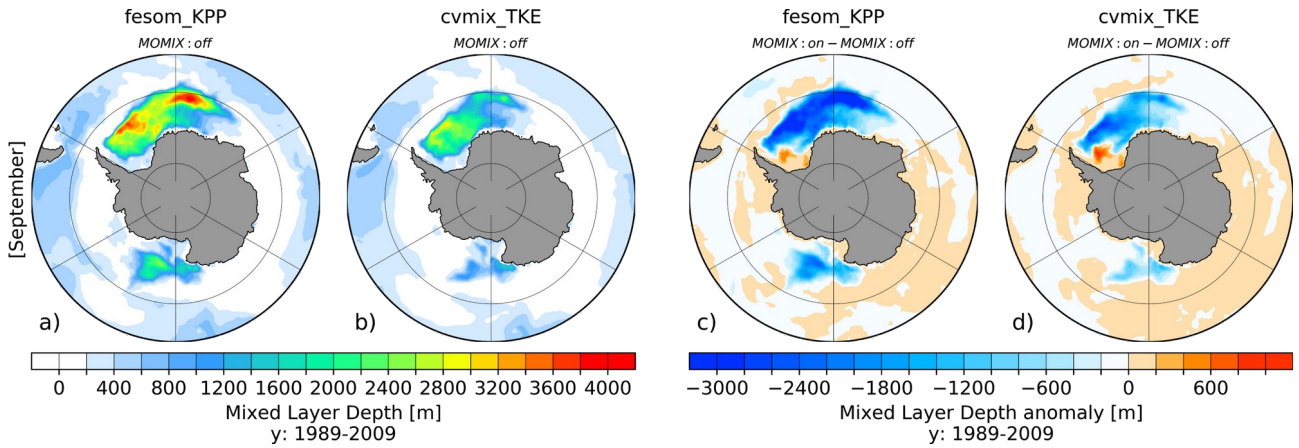
1056

1057



1058

1059 **Figure 20:** Temperature (1st and 2nd column), salinity (3rd and 4th column) difference between fesom_KPP
 1060 and cvmix_TKE vertical mixing parameterisation with Monin-Obukov vertical mixing (MOMIX) switch on
 1061 and off (MOMIX: on minus MOMIX: off) averaged for the period 1989 to 2009. From top to bottom, panels
 1062 show the vertically averaged fields for the depth ranges of 0-250 m, 250-500 m, 500-1000 m, 1000-2000 m
 1063 and 2000-4000 m.

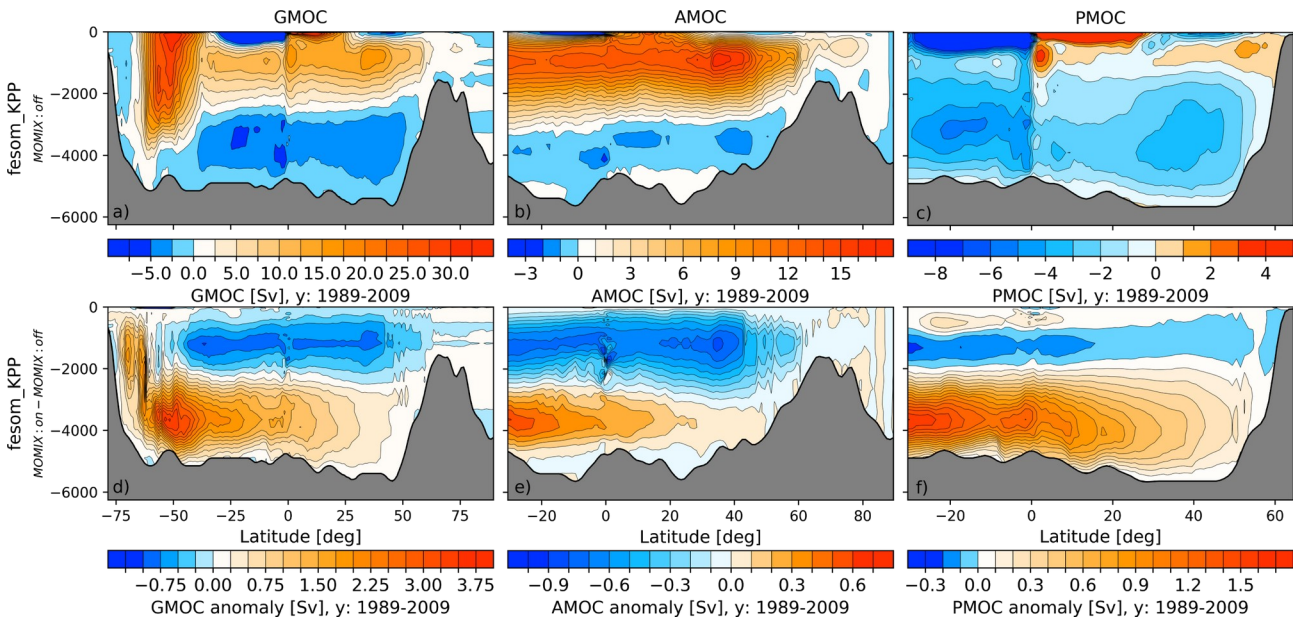


1064

1065 **Figure 21:** Southern Hemispheric September mixed layer depth (MLD) for fesom_KPP (a) and cvmix_TKE
 1066 (b) with switch off Monin-Obukov vertical mixing (MOMIX) parameterisation as well as corresponding
 1067 anomalous MLD between switched on and off MOMIX parameterisation (c, d, MOMIX: on minus MOMIX:
 1068 off), averaged for the period 1989-2009.

1069

1070



1071

1072 **Figure 22:** Absolute (upper row) and anomalous (lower row) Global (GMOC, left column), Atlantic
 1073 (AMOC, middle column) and Indo-Pacific (PMOC, right column) Meridional Overturning Circulation,
 1074 averaged for the time period 1989-2009. Absolute values are shown for fesom_KPP with switched off
 1075 Monin-Obukov vertical mixing (MOMIX) parameterisation, anomalous values show the difference between
 1076 fesom_KPP with switch on/off MOMIX parameterisation MOMIX: on minus MOMIX: off).

1077

1078